Heaving motion of a floating body

a computational approach

Michał Jan Odorczuk

Master's Thesis, Spring 2023

This master's thesis is submitted under the master's programme *Computational Science*, with programme option *Mechanics*, at the Department of Mathematics, University of Oslo. The scope of the thesis is 30 credits.

The front page depicts a section of the root system of the exceptional Lie group E_8, projected into the plane. Lie groups were invented by the Norwegian mathematician Sophus Lie (1842–1899) to express symmetries in differential equations and today they play a central role in various parts of mathematics.

Abstract

This thesis presents a comprehensive investigation of the simulation sensitivity and accuracy for small scale floating bodies in low Reynolds number regime. The study aims to provide an extensive insight into the factors and phenomena important in simulating floating rigid bodies. The work is a continuation of previous research that performed small scale experiments and aims to provide as comprehensive basis for future expansion as possible.

This paper is divided into three parts. In the first part, the experimental data is compiled and analysed, and all the most important characteristics are described. The experiments involve a wax cylinder constrained to heave motion released directly under the water surface.

The second part performs an exhaustive analysis of the process of preparing a simulation framework and lists the simulation setups utilised in this study. This part is split into four sections. The first focuses on the choice of the simulation framework and its setup. The second focuses on the stability and convergence of various simulation configurations. The third compares four different turbulence models. Finally, the fourth performs sensitivity tests for a chosen turbulence model.

Finally, the third part summarises and compares the simulation results. The stability analysis is performed and the main characteristics of the floating body motion are compared against the experimental data.

Overall, the findings of this thesis contribute to a better understanding of the small scale, low Reynolds simulated flows and the sensitivity of the numerical approach. The results of this study provide a solid basis for further development of an extensive framework for iceberg simulation.

Acknowledgements

Contents

List of Figures

List of Tables

CHAPTER 1

Introduction

Due to climate change, the receding ice in the Arctic Ocean makes new petroleum and natural gas deposits available for exploitation. According to Norsk Petroleum 2023, the Barents Sea may contain up to half of the Norwegian shelf fossil fuel deposits. While the area is predominantly ice-free throughout the year, it is still at risk of iceberg impact.

Global warming also accelerates iceberg formation and its deterioration. This lowers the average iceberg size and load on impact. It increases, however, the probability of an impact by small to medium icebergs. Keghouche, Bertino and Lisæter 2009 identified five primary iceberg source points in the Barents Sea: Edgeøya, Nordauslandet, Novaya Zemlya, Zemlya Georga and Wilczek Land. Many of these icebergs are carried across the Barents Sea by sea currents and winds (see Odorczuk and Chanrion 2022), requiring proper ice management for any structures built in the area.

Keghouche, Bertino and Lisæter 2009; Lichey, Harmut and Hellmer 2001 have provided formulas for iceberg movement that consider the impact of the air, water, Coriolis force, interaction with sea ice surface, wave radiation stresses, and pressure gradient force. Using those, Odorczuk and Chanrion 2022 implemented a simple example of a simulator with a naïve assumption of a constant iceberg surface profile and orientation.

In understanding the behaviour of forces, the profiles of both submerged and exposed iceberg surfaces are crucial. As icebergs move in waves, their profiles change due to heaving and pitching. Estimating these changes is possible with three sources of information: observation data, which is limited; experimental data using miniature models, which is time-consuming and may not be scalable; and numerical simulation, which requires extensive knowledge of natural phenomena and may be prone to numerical errors.

Icebergs are complex objects with uneven surfaces and cavities, which can lead to variations in density. In addition, they move through an unstable environment with currents, winds, and waves and experience heaving, pitching, and rolling. Creating a comprehensive simulation of this behaviour requires addressing numerous complex subproblems. Initial development steps should simplify the task by constraining movement, creating a uniform density distribution, removing the impact of waves, winds, and currents by creating a static environment, and utilising a simple two-dimensional shape.

The thesis at hand delves into the analysis of a numerical approach that is then compared to experimental data. Owing to the complexity of the problem, only a few scenarios will be covered. Extensive preliminary studies on multiple

lightweight cases are necessary to simulate full-scale complex shape three-dimensional objects. The initial phase involves simulating and analyzing simple scenarios, progressively building upon them.

These scenarios involve two-dimensional cylindrical objects with a density similar to ice. The analysis will only consider the heave motion of initially fully submerged cylinders. Future studies may include similar scenarios with waves, three-dimensional space and more intricate geometries.

The source code for the simulations performed for this thesis is publicly available at https://github.com/MJOdorczuk/FloatingObjectOpenFOAM.

CHAPTER 2

Literature

This chapter summarises various literature sources used as a basis for this paper. While analysing the main subject, several fundamental problems must be handled; for example, Greenhow 1988; Moyo and Greenhow 2000; Takamure and Uchiyama 2020 demonstrate experimental approaches to air-water interface breaking by upward object movement. Battistin and Iafrati 2003; Greenhow 1987; Greenhow 1988; Lewis et al. 2010; T. Sun et al. 2021; Zhao and Faltinsen 1993 show an analogous case for water entry. Numerical approaches to these problems can be found, for example, in Battistin and Iafrati 2003; Greenhow 1987; Greenhow 1988; Mei, Liu and Yue 1999; Moyo and Greenhow 2000; Nguyen, Ha and Park 2013; G. Wu, H. Sun and He 2004; Zhao and Faltinsen 1993.

This thesis also builds upon results and conclusions from scientific papers on submerged body movement (like Eldredge 2007; Gilmanov and Acharya 2008; Gilmanov and Sotiropoulos 2005; Henry 2013; Shen, Chan and Lin 2009), wave-body interactions (Calderer et al. 2014; Elias 2015; Li and Bachynski 2019; Lin 2007; Yang and Stern 2009) and heave decay (Itō 1977; Kramer et al. 2021).

2.1 Water entry and exit experiments

Experiments on water entry and exit mechanisms used different body models. Common shapes were spheres, cylinders, and wedges. Most articles used materials denser than water, usually from $2 \times 10^3 \, \mathrm{kg \, m^{-3}}$ to $8 \times 10^3 \, \mathrm{kg \, m^{-3}}$.

Spherical object

Several studies researched both water entry and exit of spherical bodies. Takamure and Uchiyama 2020; Truscott, Epps and Munns 2016; Q. Wu et al. 2017 examined the impact of the water exit of a sphere launched vertically upwards. Takamure and Uchiyama 2020 utilised a sphere of density $2.64 \times 10^3 \, \mathrm{kg \, m^{-3}}$ and diameter 25.4 mm, with the sphere breaking the interface with $Re \approx 3000$. Truscott, Epps and Munns 2016 employed ping pong balls with negligible density compared to water and Reynolds number at the exit ranging from 4×10^4 to 6×10^5. Finally, Q. Wu et al. 2017 used two balls, one hollow aluminium sphere density of $1.6 \times 10^3 \, \mathrm{kg \, m^{-3}}$ and diameter of 150 mm and one hollow stainless steel sphere density of $1 \times 10^2 \, \mathrm{kg \, m^{-3}}$ and diameter of 140 mm. Both exiting water with a velocity of $0.5 \, \mathrm{m \, s^{-1}}$, resulting in a Reynolds number of $\approx 5 \times 10^4$.

Takamure and Uchiyama 2020 analysed the energy loss and water sheet shape at the breaking moment. Truscott, Epps and Munns 2016 obtained results on pop-up height for high exit velocities with both fully vertical and oscillatory regimes. Q. Wu et al. 2017 showed the relationship between the water exit behaviours and the Froude number for both forced and free water exits.

Ahmadzadeh et al. 2014; May 1951 performed analogous experiments with a sphere water entry. May 1951 performed experiments with releasing steel spheres of varying roughness from different levels to obtain a specific entry speed. Ball diameters ranged from 0.125 in to 3 in, approximately 3.18 mm to 76.2 mm, and entry speed ranged from 5 ft/s to 22 ft/s, approximately $1.52\,\mathrm{m\,s^{-1}}$ to $6.71\,\mathrm{m\,s^{-1}}$. Ahmadzadeh et al. 2014 focused on a numerical approach with validation by experimental data for spheres of diameter 25.4 mm impacting water with velocity $2.17\,\mathrm{m\,s^{-1}}$. Four materials were considered, polypropylene of density 0.86 that of water, nylon of density 1.14 that of water, Teflon of density 2.30 that of water, and steel of density 7.86 that of water.

May 1951 focused on cavity formation depending on the sphere's surface roughness. They concluded that scaling has little impact on the cavitation and that cavitation occurs at much lower velocities for contaminated surfaces. Ahmadzadeh et al. 2014 compares numerical model results on cavity formation to experimental measurements using a coupled Eulerian-Lagrangian model provided by ABAQUS software.

Furthermore, a water tank experiment was performed and compared to several different simulation approaches by Kramer et al. 2021. 11 simulation configurations were used, 5 RANS models, 4 LPF models and a single FNPF model, both latter being LES models. Three of the five RANS cases utilised no turbulence model, and two employed k-Omega SST.

Cylinder

Spherical objects are three-dimensional cases that cannot do not simplify trivially into a two-dimensional one, unlike a cylindrical body. Greenhow 1988 researched such an example. Both water entry and exit are considered and compared to numerical solutions. Only Froude numbers ($Fr = 0.082$ and 0.51) and the initial positions of the cylinder are provided, with no mass or density.

Wedge

Another two-dimensional shape is a wedge. Greenhow 1987; Lewis et al. 2010; G. Wu, H. Sun and He 2004 researched this case. Both Greenhow 1987; G. Wu, H. Sun and He 2004 analysed a jet formed by a wedge impacting water and utilized similarity solutions. Meanwhile, Lewis et al. 2010 shared the findings from an experiment involving the impact of a wedge, which was recorded using a high-speed camera.

2.2   Numerical models

Although extensive scientific literature exists on numerical schemes and models, there is no need to focus extensively on the mathematical background of those. Most of the required knowledge base is accessible within online documentation

for various numerical tools. Online 2023 is a vast collection of articles on fluid dynamics numerical methods. Moreover, various CFD tools, like OpenCFD 2023; Popinet et al. 2013–2023, offer encyclopedias.

Several companies offer specialised workshops in numerical tools. Guerrero 2022 provided the author of this thesis with free learning materials and code examples for dynamic meshes in OpenFOAM. Within these, they also explain the influence of different numerical schemes on the simulation results.

CHAPTER 3

Experimental approach

This chapter explains the data obtained from the University of Oslo experiments. These experiments include several setups of cylindrical bodies constrained to heave motion either released under water or dropped above the surface.

3.1 Experimental setup

All cases mentioned below used the same configuration. The tank used for the experiment was $1.5\,\text{m}$ in length and $0.4\,\text{m}$ in width. The floating object was a wax candle $0.243\,\text{m}$ in length and $0.059\,\text{m}$ in diameter. Figure 3.1 illustrates the experimental setup with a cylinder fixed on two hollow carbon fibre rods sliding on air bearings. The total mass of the candle-rods system was measured to be $621\,\text{g}$. No significant friction was measured with the air bearings.
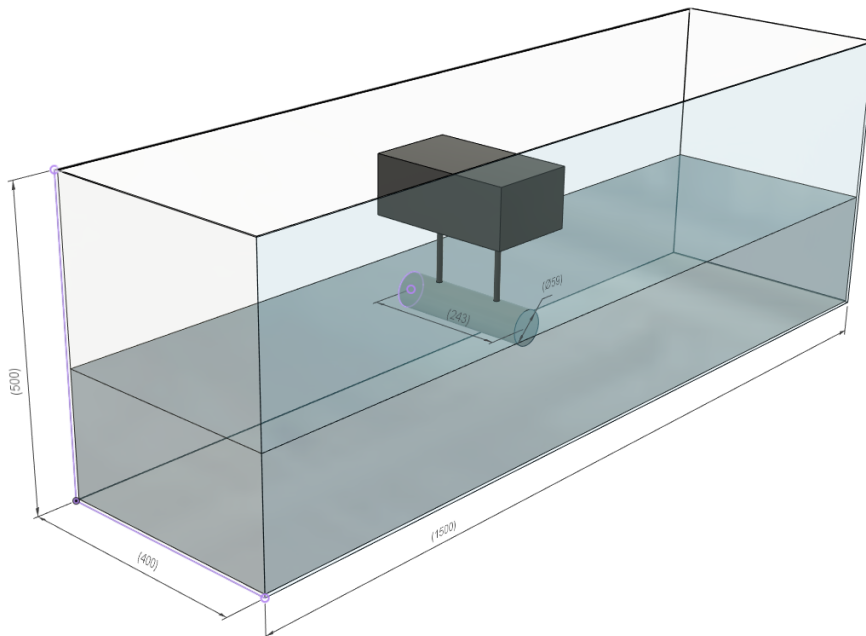
Figure 3.1: The experimental setup. Wax cylinder constrained to heave motion by two hollow carbon fibre rods sliding on air bearings.
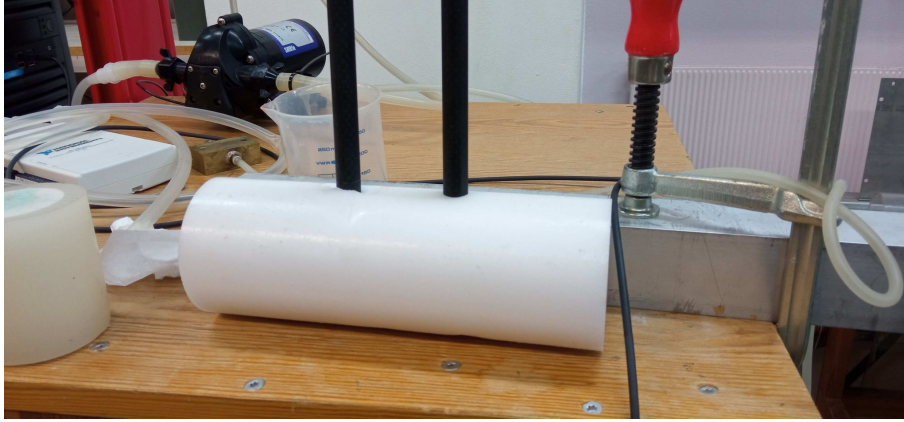
Figure 3.2: Wax candle used as the cylindrical floating body in the experiment. The diameter of the candle is 59 mm and the length is 243 mm. The shape is visibly nonuniform.

diameter	59 mm
initial heave position	-29.5 mm
water depth	205 mm
length	243 mm
mass	621 g

Table 3.1: Parameters of the cylinder used in experimental cases 51, 52 and 53.

Figure 3.2 displays the heaving system setup. The candle is not a perfect cylinder, thus the volume may vary from the nominal. The floating object did not have any contact with the tank's walls and the movement was constrained to heave motion only.

3.2 Submerged cylinder

This section explains and analyses data obtained from the experiments on the heave of a submerged cylinder in the initially still water. According to Table 3.1, the density of the cylinder is $\rho = 934.74 \, \text{kg} \, \text{m}^{-3}$. These are only the nominal dimensions. The most unreliable measurement is the diameter as the surface is highly irregular. Furthermore, the candle is not perfectly flat at the ends, leading to faults in measuring the length. Also, the initial heave position with respect to the water surface might have differed from the nominal.

Three experiments were conducted and labelled as '51', '52' and '53' (see Figures A.1 to A.3, respectively. For the comparison from the release point, see Figure A.4). The cylinder used in the experiments was fully submerged under the water surface and released after the surface became calm. The sampling frequency used for the experiments was 2 kHz.

Only the first three seconds of each experiment were considered to avoid the influence of wave reflection. Each experiment's relevant part of the time series is shown in Figure 3.3, but the data is visibly noisy due to sensor inaccuracies. New time series were created by smoothing the original data using a uniform
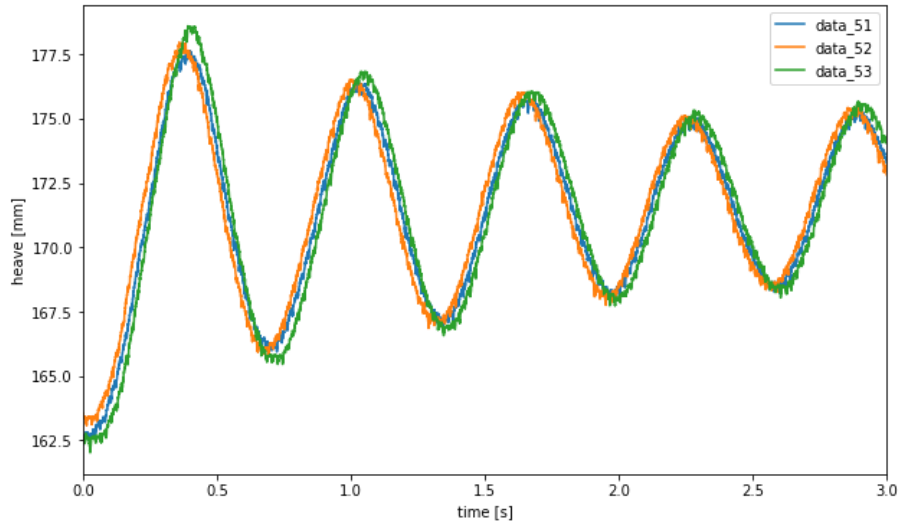
Figure 3.3: Comparison of the heave evolution throughout the first 3 seconds for the cases '51', '52' and '53'.
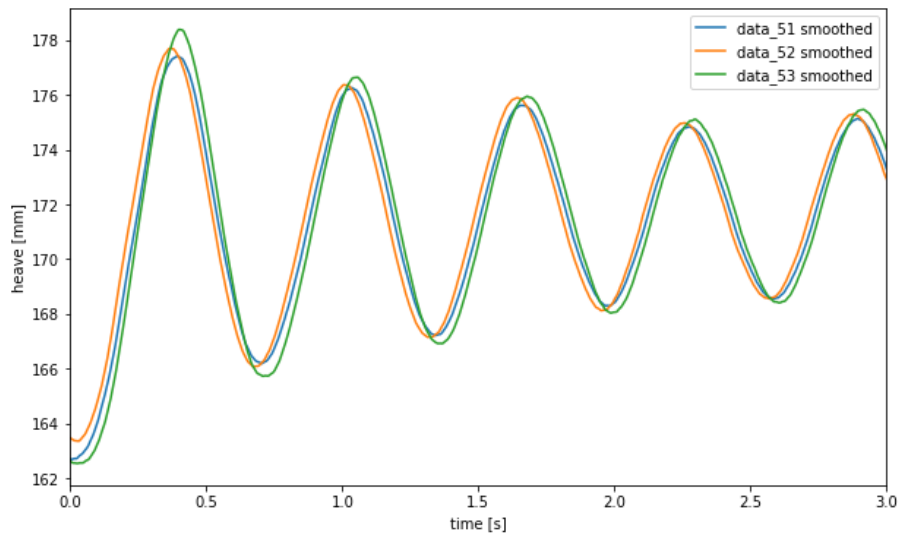
Figure 3.4: Comparison of the heave evolution through the first 3 seconds for the cases '51', '52' and '53'. Samples smoothed by a convolution with a uniform mask of length 100.

convolution mask of length 100, simplifying the analysis, as seen in Figure 3.4.

The initial heave positions in the experiments are 162.69 mm, 163.47 mm and 162.63 mm for '51', '52' and '53' respectively. From these and the stable positions 171.92 mm, 171.92 mm and 171.83 mm the differences between the initial positions and the stable positions are 9.22 mm, 8.46 mm and 9.2 mm respectively. This further gives the final stability positions at 20.28 mm, 21.04 mm and 20.3 mm below the water surface.
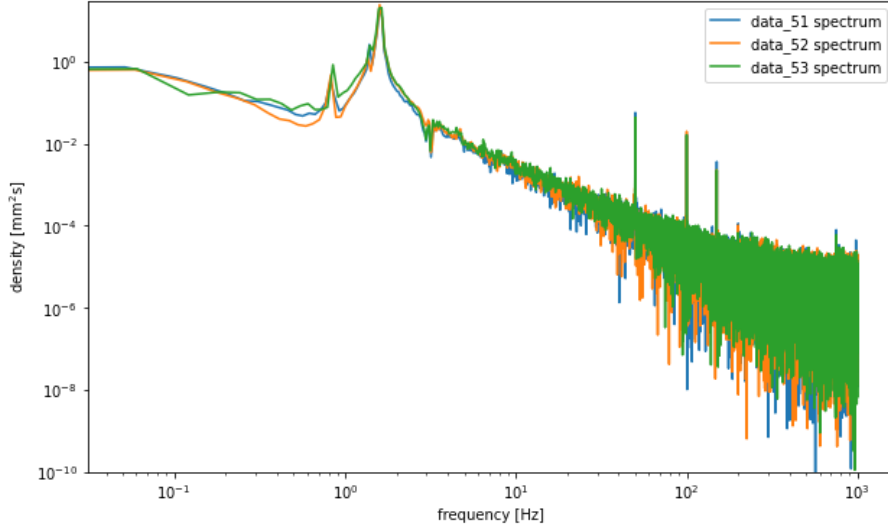
Figure 3.5: Power spectral density of time series for the cases '51', '52' and '53' for the entire time series past the release.

As the cylinder used for the experiment was not uniform in shape, only the mass can be assumed to be precisely measured. Thus, from hydrostatic balance

$$\rho_c \pi r^2 = \rho_a C_a + \rho_w C_w, \tag{3.1}$$

where ρ_c is the density of the cylinder, ρ_a is the density of air $(1\,\mathrm{kg\,m^{-3}})$, ρ_w is the density of water $(998.2\,\mathrm{kg\,m^{-3}})$, C_a is the face area above the water surface and C_w is the face area under the water surface, where $C_a + C_w = \pi r^2$.

$$C_w = r^2 \arccos\left(\frac{-h}{r}\right) + h\sqrt{r^2 - h^2} \tag{3.2}$$

with h being the height of the centre of mass of the cylinder. Setting $h' = \frac{h}{r}$ normalises and simplifies the equation by removing r. Thus

$$\rho_c = \frac{\rho_a}{\pi}\left(\arccos\left(-h'\right) + h'\sqrt{1 - h'^2}\right) + \frac{\rho_w}{\pi}\left(\pi - \arccos\left(-h'\right) - h'\sqrt{1 - h'^2}\right). \tag{3.3}$$

Setting the values of h' it gives the density of the cylinder $898.49\,\mathrm{kg\,m^{-3}}$, $910.16\,\mathrm{kg\,m^{-3}}$ and $898.8\,\mathrm{kg\,m^{-3}}$, all of which are noticeably lower then the one provided. That can be the result of either faulty measurements, or inconsistent radius. Assuming the radius and mass to be correct, the length of the cylinder becomes $252.77\,\mathrm{mm}$, $249.43\,\mathrm{mm}$ and $252.68\,\mathrm{mm}$ respectively.

Characteristics of the movement

Figure 3.5 presents the power spectrum densities for all the cases. For all a peak can be seen at similar frequencies. That is at $1.593\,\mathrm{Hz}$, $1.593\,\mathrm{Hz}$ and $1.64\,\mathrm{Hz}$ for '51', '52' and '53' respectively. It is noteworthy, that for the first $3\,\mathrm{s}$ these

9

no.	case 51		case 52		case 53	
	time [s]	heave [mm]	time [s]	heave [mm]	time [s]	heave [mm]
1	0.0025	−9.5419	0.0135	−8.8463	0.0270	−9.8042
2	0.3900	5.7193	0.3595	6.0431	0.3920	6.7688
3	0.7240	−5.9780	0.6910	−6.1352	0.7275	−6.3716
4	1.0270	4.4731	0.9970	4.6001	1.0380	4.9978
5	1.3430	−4.9285	1.2905	−5.0638	1.3470	−5.2565
6	1.6375	3.8171	1.6365	4.0972	1.6625	4.2107
7	1.9665	−3.8572	1.9525	−4.1674	1.9670	−4.0977
8	2.2965	3.1175	2.2480	3.2008	2.2800	3.4892
9	2.6020	−3.7041	2.5905	−3.6645	2.6055	−3.7916
10	2.8970	3.3361	2.8560	3.5069	2.8940	3.8390

Table 3.2: Consecutive crests and troughs in experimental cases 51, 52 and 53.

no.	case 51		case 52		case 53	
	Δ time [s]	heave [unit]	Δ time [s]	heave [unit]	Δ time [s]	heave [unit]
1	0.0025	−1.0000	0.0135	−1.0000	0.0270	−1.0000
2	0.3875	0.5994	0.346	0.6831	0.365	0.6904
3	0.334	−0.6265	0.3315	−0.6935	0.3355	−0.6499
4	0.303	0.4688	0.306	0.5200	0.3105	0.5098
5	0.316	−0.5165	0.2935	−0.5724	0.309	−0.5361
6	0.2945	0.4000	0.346	0.4632	0.3155	0.4295
7	0.329	−0.4042	0.316	−0.4711	0.3045	−0.4180
8	0.33	0.3267	0.2955	0.3618	0.313	0.3559
9	0.3055	−0.3882	0.3425	−0.4142	0.3255	−0.3867
10	0.295	0.3496	0.2655	0.3964	0.2885	0.3916

Table 3.3: Normalised crests and troughs in experimental cases 51, 52 and 53. First trough position set as −1.

values are the same, equal to 1.6667 Hz. The extrema occurring in these cycles are listed in Table 3.2 and plotted in Figure 3.6.

To normalise the data, all the heave positions in Table 3.3, are represented as a fraction of the initial low position. Moreover, time differences between each extremum are given.

The average periods for each case are: 0.6499 s, 0.6443 s and 0.6446 s giving respectively 1.5387 Hz, 1.5521 Hz and 1.5521 Hz frequency. It is noteworthy that the leading frequencies are not equivalent to the oscillation frequency. The deterioration of the amplitude is shown in Figure 3.6. To better illustrate the damping, Table 3.4 contains heave positions in the extrema as fractions of the last extremum of the same type.

Another characteristic value is the velocity with which the cylinder heaves. Its maxima and minima represent the points of equilibrium. Figure 3.7 shows the comparison between all three data sets. The points of equilibrium are shown in the table below.

no.	case 51	case 52	case 53
3	0.6265	0.6935	0.6499
4	0.4688	0.5200	0.5098
5	0.8244	0.8254	0.8249
6	0.8532	0.8908	0.8425
7	0.7825	0.8230	0.7797
8	0.8167	0.7811	0.8286
9	0.9604	0.8792	0.9251
10	1.0701	1.0956	1.1003

Table 3.4: Extrema of the heave of the floating object as a fraction of the previous extremum of the same type.
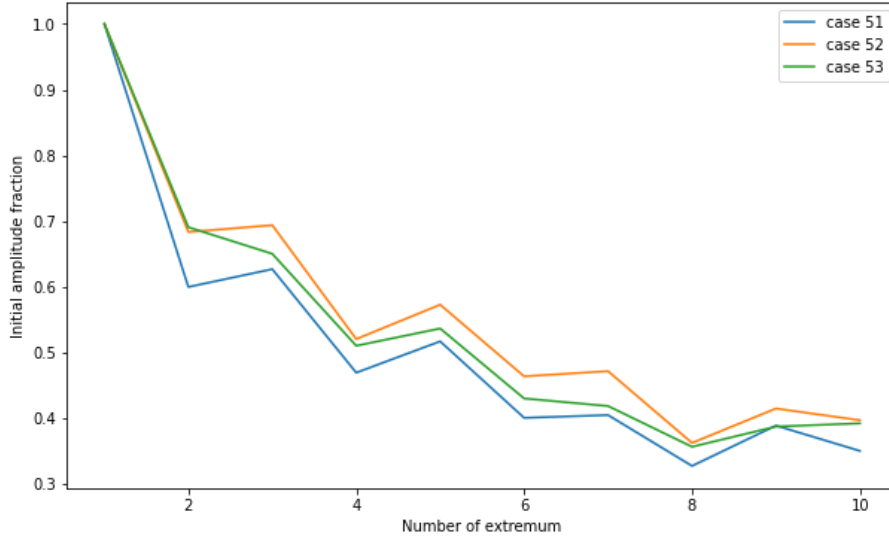
Figure 3.6: Amplitude deterioration with each extremum, minima are odd, maxima are even.

	case 51		case 52		case 53	
no.	time	heave	time	heave	time	heave
	[s]	[mm]	[s]	[mm]	[s]	[mm]
1	0.2690	1.1060	0.1785	−2.8993	0.1925	−4.5131
2	0.5385	−0.1403	0.5070	0.6864	0.5425	0.5594
3	0.8680	−0.9711	0.8780	0.5990	0.8925	−0.5557
4	1.1775	0.1440	1.1690	−0.5380	1.2010	−0.1840
5	1.4680	−1.8894	1.4765	−0.8003	1.4930	−1.4521
6	1.8175	−0.0091	1.7665	1.2549	1.8215	0.7124
7	2.1100	−0.7743	2.0975	−0.6473	2.1335	−0.5338
8	2.4370	−0.6432	2.4260	−0.8003	2.4615	−0.6869
9	2.7295	−0.4901	2.7160	−0.2975	2.7705	0.5157

Table 3.5: Consecutive equilibrium points in experimental cases 51, 52 and 53.
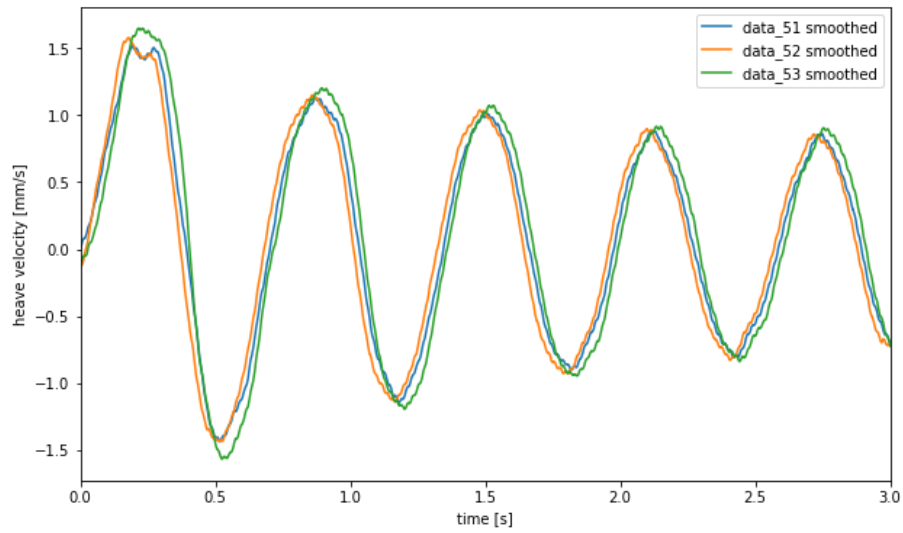
Figure 3.7: Comparison of the heave velocity evolution through the first 3 seconds for the cases '51', '52' and '53'. Samples smoothed by a convolution with a uniform mask of length 100.

3.3 Other experiments

Because of the time limitations for this thesis, only the first simulation setup is utilised in the simulations. There were more experiments performed, like a cylinder released directly from the water surface level or up from the height equal to one cylinder radius. These will be surveyed as a part of further research which should lead to a full iceberg simulation.

CHAPTER 4

Computational approach

This chapter concentrates on the computational aspect. Thus it is crucial to choose a framework to use for the simulations. To keep the workload manageable, already existing software is used. Moreover, no paid software like ABAQUS (as used, for example, by Ahmadzadeh et al. 2014) is considered because of no funding for this project. Only open-source applications are analysed, namely, OpenFOAM (see OpenCFD 2023) and Basilisk (see Popinet et al. 2013–2023).

There are two problems to be solved. First is multiphase flow with surface penetration. The second is rigid body movement. Both applications offer several solvers for both of these problems.

4.1 Multiphase flow solvers

OpenFOAM

OpenFOAM offers several solvers for various subproblems (see CFD Direct Ltd 2015–2023):

- `cavitatingFoam` for cavitation,

- `compressibleInterFoam`, `compressibleMultiphaseInterFoam`, `interFoam`, `interMixingFoam`, `interPhaseChangeFoam`, and `multiphaseInterFoam` for capturing interfaces via volume of fluid (VOF) method,

- `driftFluxFoam` for drift-flux approximation for relative motion of the phases,

- `multiphaseEulerFoam`, `reactingMultiphaseEulerFoam`, and `twoPhaseEulerFoam` for compressible fluids with heat transfer,

- `potentialFreeSurfaceFoam` for cases with consistent wave height field,

- `twoLiquidMixingFoam` for mixing two incompressible fluids.

The buoyant body heave case does not involve significant cavitation, drift-flux approximation, or mixing. However, it does include instances of wave breaking, which can cause inconsistencies in the wave-height field. Only those from the second group are adequate when comparing solvers for incompressible fluids.

The solvers `interFoam` and `multiphaseInterFoam` are the only ones applicable, as the first two work with compressible fluids, `interMixingFoam` focuses on miscible fluids, and `interPhaseChangeFoam` deals with phase-changing fluids. Since the experiment only involves two phases, the simulator is limited to using the `interFoam` solver.

OpenFOAM in-built tutorials include three categories:

- Large Eddy Simulation with a single tutorial, two-dimensional nozzle flow,

- Reynolds Averaged Navier-Stokes with twelve examples:

  – Duisburg Test Case from Moctar, Shigunov and Zorn 2012 of a post-Panamax container ship model, both stationary and moving cases. One case includes waves.
  – Angled duct,
  – Dam breaking,
  – Dam breaking with porous baffle,
  – Electrostatic deposition,
  – Floating object,
  – Mixer,
  – Motorbike,
  – Water channel,
  – Weir overflow.

- fourteen laminar flow examples:

  – Capillary rise,
  – Dam breaking,
  – Dam breaking with permeability,
  – Dam breaking with an obstacle,
  – Two-dimensional mixer vessel,
  – Oscillating box,
  – Sloshing cylinder,
  – Sloshing two-dimensional tank,
  – Sloshing two-dimensional tank with three degrees of freedom,
  – Sloshing three-dimensional,
  – Sloshing three-dimensional with three degrees of freedom,
  – Sloshing three-dimensional with two degrees of freedom,
  – Tube mixer,
  – Wave.

This thesis describes simulating buoyant objects at the intersection of two fluids. Thus, the Duisburg Test Cases, the *floating object*, and the oscillating box tutorials are the most suitable.

Basilisk

Basilisk documentation includes a two-phase flow solver that couples the Navier-Stokes solver with the volume of fluid method. The example cases are:

- Atomisation of a pulsed jet,

- Bubble rising in a large tank,

- Transcritical flow over a bump,

- Two-phase flow around RV Tangaroa,

- Flow in a rotating bottom-driven cylindrical container.

None of them includes an inertial rigid body.

OpenFOAM is an excellent foundation for conducting research. Various authors have utilised OpenFOAM methods in their simulations, such as an elastic body springing and whipping on the water surface (Seng, Jensen and Malenica 2014), a heaving buoy (Devolder et al. 2015), sphere heave decay (Kramer et al. 2021), and the interaction of irregular waves with a two-dimensional body (Li and Bachynski 2019). Thus, this study can build upon previous research and utilise these projects' published data and configurations.

4.2 Simulation configuration

The simulations expand on the `floatingObject` tutorial from the `multiphase\interFoam\RAS` group, which includes a multiphase flow and a rigid body. The tutorial consists of three directories:

1. `0\` - containing initial fields data:

   - `alpha.water.orig` - boundary conditions for water fraction, later set to specific values by `setFields` and saved into `alpha.water`, both the walls and the floating object are set to zero gradient boundary condition, and the atmosphere is of type inletOutlet with values set to 0.

   - `epsilon` - boundary conditions and field values for turbulent kinetic energy dissipation rate. Both the walls and the floating object are set to epsilonWallFunction type with the model coefficient for the turbulent viscosity $C_\mu = 0.09$, von Kármán constant $\kappa = 0.41$, wall roughness parameter $E = 9.8$ and value set to 0.1. The atmosphere patch is of type inletOutlet with a value of 0.1. The exact value is set for the internal field.

   - `k` - turbulent kinetic energy boundary conditions and field values. The wall and the floating object are set to kqRWallFunction with a value 0.1. The exact value is set for the atmosphere patch of type inletOutlet and the internal field.

- $\bullet$ `nut` - turbulent viscosity boundary conditions and field values. All the boundary condition coefficients are set to the same as in ϵ, both the wall and the floating object are set to nutkWallFunction type, the atmosphere patch is set to calculated type, and the value everywhere is set to 0.

- $\bullet$ `p_rgh` - hydrostatic pressure boundary conditions and field values. For the wall and the floating object, the type is set to fixedFluxPressure with both the gradient and the value set to 0. The atmosphere patch is set to totalPressure type with density rho set to rho, pressure coefficient psi set to none, the ratio of specific heats $\gamma = 1$, initial pressure $p_0 = 0$ and the value equal 0. The internal field is also set to 0.

- $\bullet$ `pointDisplacement` - displacement of the mesh points set everywhere as a fixed value $(0, 0, 0)$ except for the floating object of type calculated.

- $\bullet$ `U` - boundary conditions and field values of the fluid velocity field. Initially, the whole system is stationary. Thus velocity is set to zero everywhere. Walls are set to no-slip condition, the atmosphere patch is set to pressureInletOutletVelocity type, and the floating object is set to movingWallVelocity type.

2. `constant\` - containing the constant values and conditions for the system:

- $\bullet$ `dynamicMeshDict` - dictionary for dynamic meshing. Defines mesh as dynamicMotionSolverFvMesh, with a solver rigidBodyMotion from `librigidBodyMeshMotion.so`. The rigid body motion coefficients include:

  - Report flag set to on,
  - Solver set to Newmark (see Newmark 1959),
  - Acceleration relaxation coefficient set to 0.7,
  - Rigid bodies subdictionary including one body, floatingObject, with a type cuboid, parent set to root, mass calculated as $rho \cdot Lx \cdot Ly \cdot Lz$, where $rho = 500, Lx = 0.3, Ly = 0.2, Lz = 0.5$, L set to (Lx, Ly, Lz), the centre of mass set to $(0, 0, 0.25)$, transform set to $(1, 0, 0, 0, 1, 0, 0, 0, 1), (0.5, 0.45, 0.1)$ and a composite of a prismatic and a rotational joints in the y-axis. Moreover, the patches are set to (floatingObject), and the inner and outer distances for mesh bending are set to 0.05 and 0.35, respectively.

  There is also the `dynamicMeshDict.sixDoF` file in the same directory, which provides an alternative implementation with a sixDoFRigidBodyMotion solver. It is not used by default, however.

- $\bullet$ `g` - a dictionary containing a single entry of gravitational acceleration with the value set to $(0, 0, -9.81)$,

- $\bullet$ `momentumTransport` - a dictionary containing simulation type set to RAS (Reynolds Averaged Simulation) with parameters set to kEpsilon model (see Online 2011), turbulence set to on and printCoeffs set to on,

16

- transportProperties - a dictionary containing transport coeffi-
cients for air and water phases. Both models are Newtonian with kin-
ematic viscosity ν set to $1\times10^{-6}\,\mathrm{m^2\,s^{-1}}$ for air and $1.48\times10^{-5}\,\mathrm{m^2\,s^{-1}}$
for water and density ρ set to $1\,\mathrm{kg\,m^{-3}}$ for air and $998.2\,\mathrm{kg\,m^{-3}}$ for
water.

3. system\ - containing the application descriptions for all the simulation
   segments:

   - blockMeshDict - dictionary describing the initial domain as a cube
     of size $1\,\mathrm{m^3}$ with simple uniform grading, 20 in x- and y-axes and 30 in
     the z-axis. The upper wall of the cube is set as an atmosphere patch.
     The remainder is set as stationaryWall walls, and floatingObject is
     set to have no faces but to be of type wall.

   - controlDict - dictionary describing simulation timespan and output.
     The application is set to interFoam. Simulation goes for time $0\,\mathrm{s}$
     to $6\,\mathrm{s}$ with time step $0.01\,\mathrm{s}$. Every $0.1\,\mathrm{s}$, a snapshot is saved in a
     binary format with a precision of 12 with no compression. The
     time step is set to adjustable with the maximum Courant number,
     interface Courant number and time delta all set to 1. Moreover, the
     rigidBodyState function is imported from librigidBodyState.so.

   - fvSchemes - a dictionary containing scheme options:
     - Double time derivative is set to Crank-Nicolson scheme with
       coefficient set to 0.9 (see Crank and Nicolson 1947b),
     - Gradient schemes set to linear Gaussian,
     - divergence schemes set to Gaussian finite volume Van Leer
       (vanLeerV, see van Leer 1974) for the velocity field as transport
       of a product of density and flux, Gaussian interface compression
       Van Leer with the coefficient set to 1 for flux transport of water
       fraction, Gaussian upwind (see Spalding 1972) for turbulent
       kinetic energy and its dissipation rate flux and Gauss linear for
       turbulent energy dissipation flux.
     - Laplacian schemes set to linear corrected Gaussian,
     - Interpolation schemes set to linear,
     - Surface-normal gradient schemes set to corrected.

   - fvSolutions - dictionary describing the solvers:
     - Water fraction solver set to smooth solver (see OpenFOAM
       Foundation 2018) with Symmetric Gauss-Seidel Smoother, alpha
       correctors set to 2 with one subcycle, MULES correction,
       iterations limited to 5, applying previous alpha corrections,
       tolerance set to 1×10^{-8} and relative tolerance set to 0.
     - Pressure correction solved with Preconditioned conjugate gradi-
       ent solver with tolerance 1×10^{-5}, relative tolerance 0 and
       the maximum number of iterations 100. The preconditioner
       is set to GAMG solver with tolerance 1×10^{-5}, relative toler-
       ance 0, smoother set to Diagonal-based Incomplete Cholesky
       Gauss-Seidel Smoother with no cache agglomeration.

17

– Hydrostatic pressure solver set to GAMG with tolerance 1×10^{-8}, relative tolerance 0.01 with Diagonal-based Incomplete Cholesky smoother. The final solver is set to Preconditioned conjugate gradient with tolerance 1×10^{-8}, relative tolerance 0 and the maximum number of iterations set to 20. The preconditioner is set to GAMG with tolerance 1×10^{-8}, relative tolerance 0, number of V-cycles set to 2 with Diagonal-based Incomplete Cholesky Gauss-Seidel smoother with two presweeps.

– For velocity, turbulent kinetic energy and dissipation rate, both solver and final solver are set to smooth solver with Gauss-Seidel smoother, tolerance 1×10^{-6} and the number of sweeps set to 1. The only difference is in the relative tolerance, where the initial solver has it set to 0.1, and the final solver has it equal to 0.

– Solving algorithm is set to PIMPLE (see OpenFOAM Wiki Contributors 2021) with no momentum predictor, the number of outer correctors set to 3, the number of correctors set to 1, and no non-orthogonal correctors, with flux correction and mesh movement outer correction.

– The relaxation factor is set to 1.

• `setFieldsDict` - dictionary for setting the initial water level. The general water level is set to 0.5368 and 0.65 in the corner $(0.7, 0.8)$ to $(1, 1)$.

• `topoSetDict` -dictionary for generating the body of the floating object. It is set as a cuboid $(0.35, 0.35, 0.1)$ to $(0.65, 0.55, 0.6)$.

There is also an unused `decomposeParDict` for parallel processing.

The `Allrun` script is running consecutively blockMesh, topoSet, subsetMesh setting floatingObject patches to those generated by topoSet, setFields and finally interFoam.

Figure 4.1 shows the initial state of the tutorial mentioned above.

4.3 Partially submerged cylinder heave in still water

In practice, a partially submerged cylinder is considered a two-dimensional case. When using the `setFieldsDict` function, only setting the water to a specific level is required. The `dynamicMeshDict` function sets the cylinder to only move along the z-axis with a prismatic constraint. The `topoSetDict` function is unnecessary, as the SnappyHexMesh function forms the cylindrical mesh. Additionally, to simplify the placement, the `blockMeshDict` function is modified so that the centre of the domain is located at point (0, 0, 0). Finally, since the case is two-dimensional, it is necessary to set the boundary conditions at the front and rear walls to `empty`, which requires additional entries in most dictionaries in the `0\` folder.
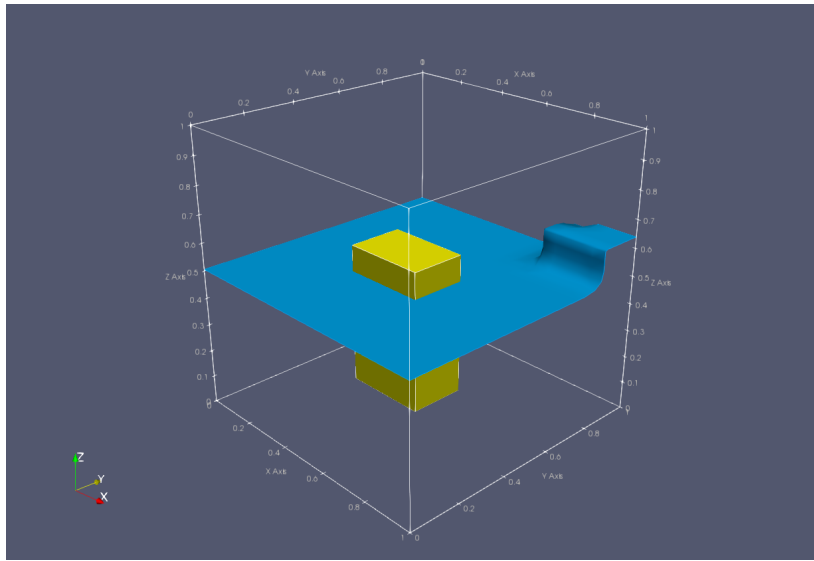
Figure 4.1: Initial state of the floating object tutorial.

Changes in the dictionary entries

setFieldDict

The only changes needed are to remove the initial corner wave and to change the water level to a single level. The new domain will span from -4 to 4 on the z-axis, with 0 being the initial water level.

blockMeshDict

The new domain for the simulation will have a range of -6 to 6 on the x-axis, with a resolution of 40 cells. On the y-axis, it will have a range of 0 to 1, with a resolution of a single cell to eliminate that dimension. The z-axis will range from -4 to 2, with a resolution of 40 cells. The initial simulation tests will use a very coarse mesh. Two new `front` and `back` patches have been added. These patches consist of two walls, normal to the y-axis, with types set to empty. The wall coordinates are $(1, 5, 4, 0)$ and $(3, 7, 6, 2)$.

0 entries

Directory `0\` was updated to include the empty boundary conditions for the new `front` and `back` patches.

dynamicMeshDict

Three modifications to `dynamicMeshDict` are:

1. The geometrical centre became the centre of mass.

2. The joint has been replaced from composite prismatic in the y-axis and rotational in the y-axis to prismatic in the z-axis.

19
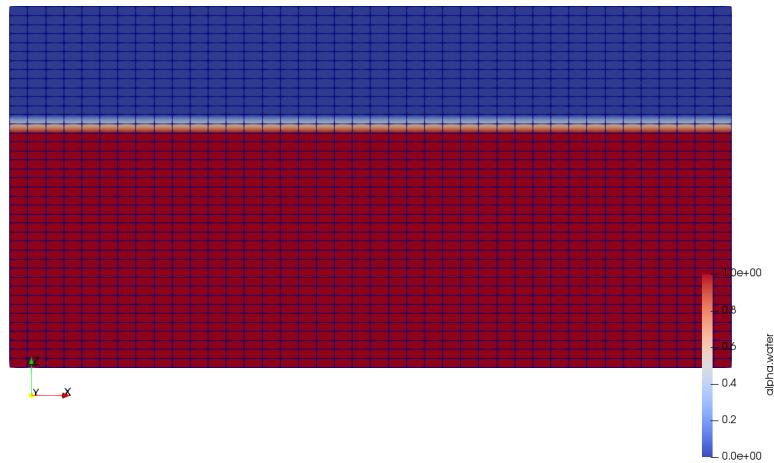
Figure 4.2: alpha.water field set with mesh overlay for no rigid body set.

3. The `outerDistance` entry has been increased from 0.35 to 2 to allow farther movements.

Figure 4.2 portrays the resulting mesh with the `alpha.water` field.

SnappyHexMesh

After setting up the initial, two-dimensional domain, the next step is for SnappyHexMesh to refine and warp the mesh around a cylinder of diameter $1\,\mathrm{m}$. The mesh used for this case is the `constant\geometry\Cylinder.stl` file. OpenFOAM offers templates of `snappyHexMeshDict` and `meshQualityDict`. Moreover, several OpenFOAM tutorials, like `mesh\snappyHexMesh\flange`, provide an example of use.

To analyse the performance of the tool, five different cases are considered:

Castellation only

In cases with only castellation (see Figures 4.3 and 4.4), the floating body assumes a cross shape of cells that land within the cylinder. Regarding the cylinder's density at $500\,\mathrm{kg\,m^{-3}}$ and the initial position at 0, a slight upward movement can be anticipated due to the negligible density of the air. However, a significant upward pull occurs due to mesh construction inaccuracies, resulting in a final heave position of around $0.07\,\mathrm{m}$.

Castellation with snapping

SnappyHexMesh snaps cell vertices to the refinement region boundaries to improve mesh quality. The resulting shape is a hexadecagon that more accurately replicates the area of a circle (refer to Figures 4.5 and 4.6). As a result, the initial heave pull during simulation is approximately four times less than in the

Figure 4.3: Initial simulation state for castellated cylinder with no snapping.
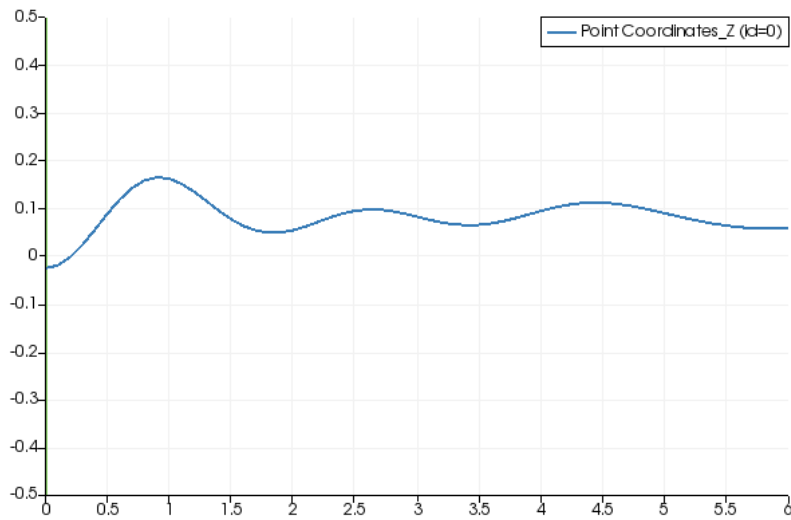
Figure 4.4: Heave progression for castellated cylinder with no snapping.
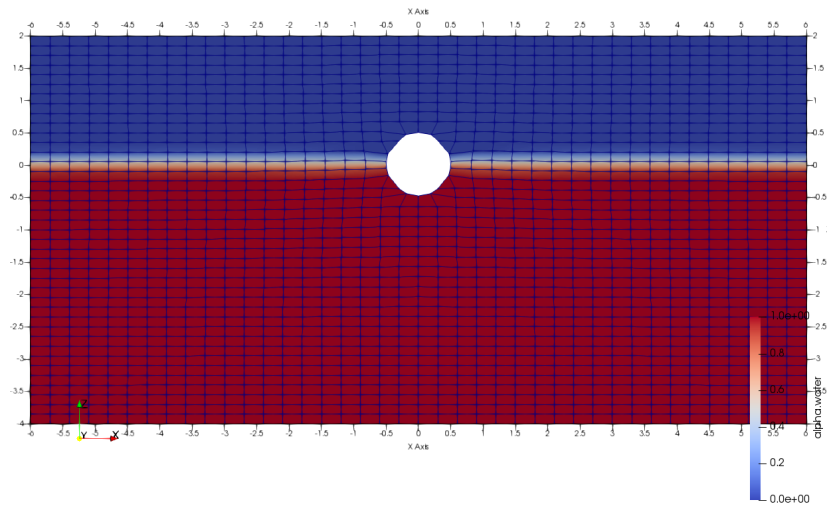
Figure 4.5: Initial simulation state for castellated cylinder with snapping.
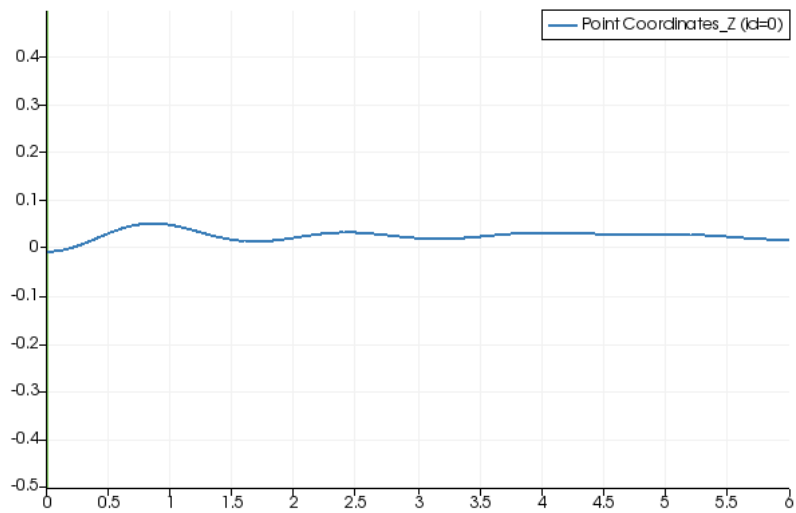
Figure 4.6: Heave progression for castellated cylinder with snapping.

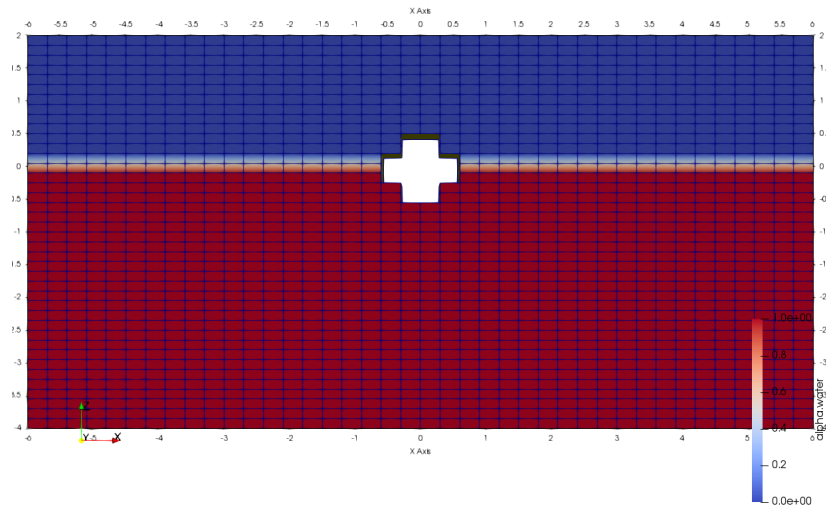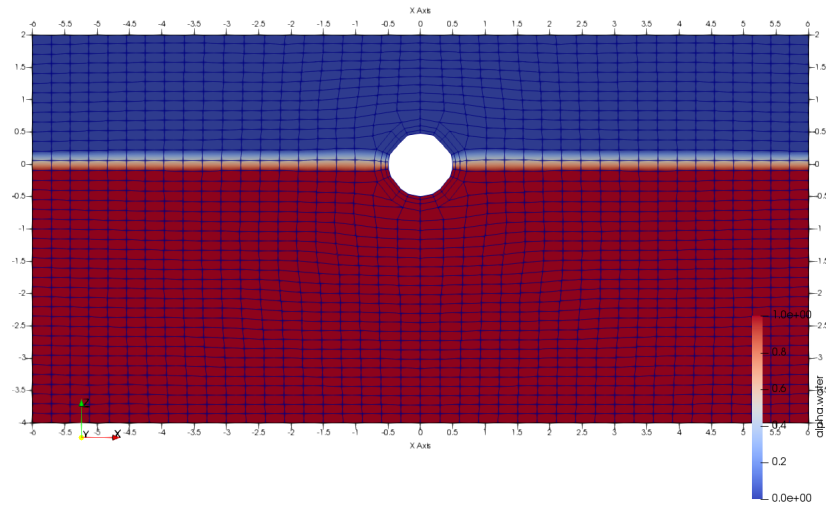Figure 4.7: Initial simulation state for castellated cylinder with snapping and added layers.
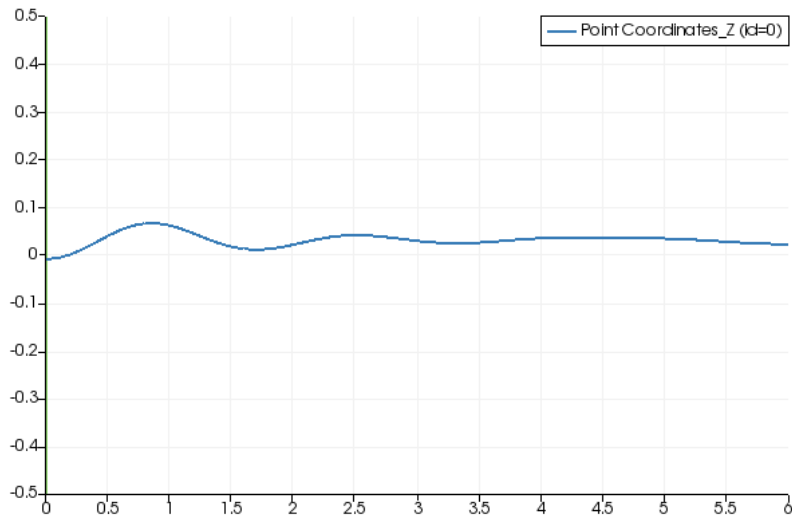
Figure 4.8: Heave progression for castellated cylinder with snapping and added layers.
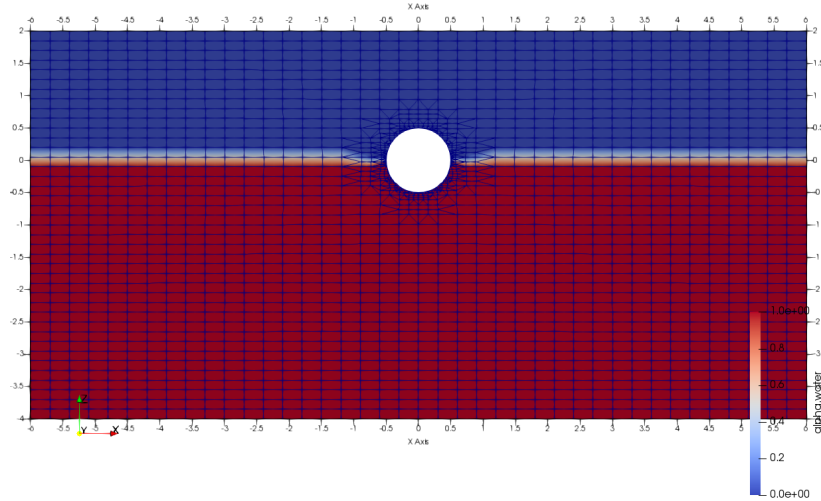
Figure 4.9: Initial simulation state for castellated cylinder with snapping, added layers and refinement of minimum level 0 and maximum level 3.

previous case, and the object's centre of mass is closer to zero in the initial frame. Eventually, the object stabilises around $0.02\,\mathrm{m}$.

Castellation with snapping and adding layers

One can utilise the `addLayers` feature to enhance mesh quality, incorporating curved cell layers around the cylinder (see Figures 4.7 and 4.8). This modification improves the accuracy of flow calculations near the surface without significantly altering the cylinder's shape. The initial pull and stable heave position are slightly elevated, indicating an increase in surface area or altered flow due to the additional layers.

Mesh refinement

In order to improve the mesh, it is necessary to refine the area surrounding the cylinder. This task requires the adjustment of the `refinementSurfaces` in the `snappyHexMeshDict\castellatedMeshControl` dictionary. The parameter `level` of `floatingObject` is set to $(0, 3)$ to refine it up to three times. Figure 4.9 presents the result. However, this modification leads to singularities and acceleration in time at $t = 0.256\,371\,\mathrm{s}$, with a z-directional speed of $-1.225 \times 10^{13}\,\mathrm{m\,s^{-2}}$ attributed to the instability of the Crank-Nicolson method (see Crank and Nicolson 1947a; Fornberg 1973).

Crank-Nicolson time scheme solves

$$\frac{u_i^{n+1} - u_i^n}{\Delta t} = \frac{1}{2}\left[\frac{f(u_{i+1}^{n+1}) - f(u_{i-1}^{n+1})}{\Delta x} + \frac{f(u_{i+1}^n) - f(u_{i-1}^n)}{\Delta x}\right] \qquad (4.1)$$

24
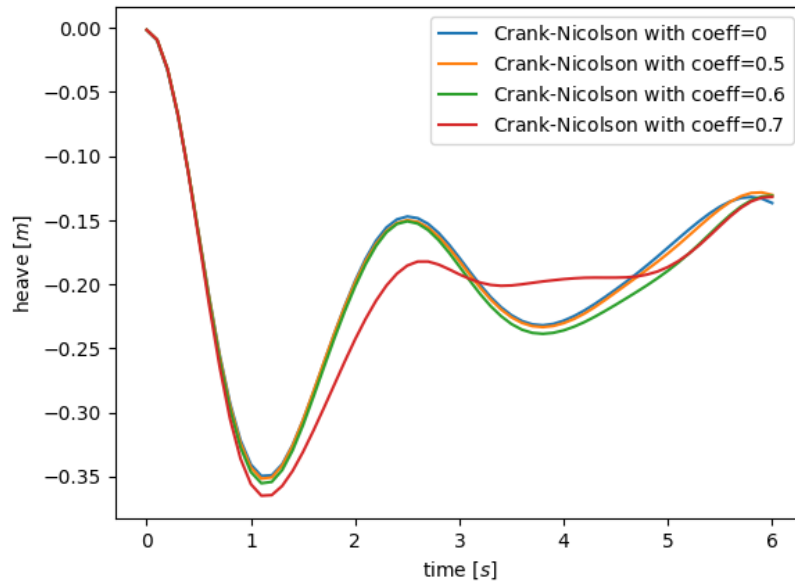
Figure 4.10: Comparison of Crank-Nicolson method resulting heave for various coefficients.

with Δt derived from Courant-Friedrichs-Lewy condition CFL $\geq U \frac{dt}{dx}$. Decreasing the coefficient CFL value is recommended to prevent stability problems.

The comparison of the heave time series with different coefficients of the Crank-Nicolson scheme is shown in Figure Figure 4.10. There is no significant difference for values up to 0.6. However, the system starts to diverge for values exceeding 0.6. At 0.8, the simulation failed at approximately $t \approx 0.45\,\mathrm{s}$ due to a strong feedback loop, resulting in a singularity. Following Kramer et al. 2021, a coefficient value of 0.5 is utilised for further simulations as a countermeasure. Nevertheless, testing with varying coefficients is imperative for different simulation configurations.

Regional mesh refinement and extrusion

In order to increase the simulation speed, one can simplify mesh in less significant areas, such as those above and below the water surface or in the far field. A searchable box named `waterLevelBox` can be created to cover the area near the water's surface. The region inside the box can then be refined by adding an entry to the `castellatedMeshControls` section and setting the refinement level to 4, dividing all cells within that region into 16 subcells in each direction. However, this approach may cause singularities due to flux perpendicular to the empty patches. The `extrudeMesh` tool addresses that issue by creating a single-cell width wall. It captures only the domain's front faces and extrudes them into the third dimension.

Furthermore, `snappyHexMesh` refines the mesh in the area of interest while coarsening it outside. The initial grading of the mesh was set to $(12, 1, 6)$ instead of $(40, 1, 40)$. This change resulted in a mesh with 2316 cells, where
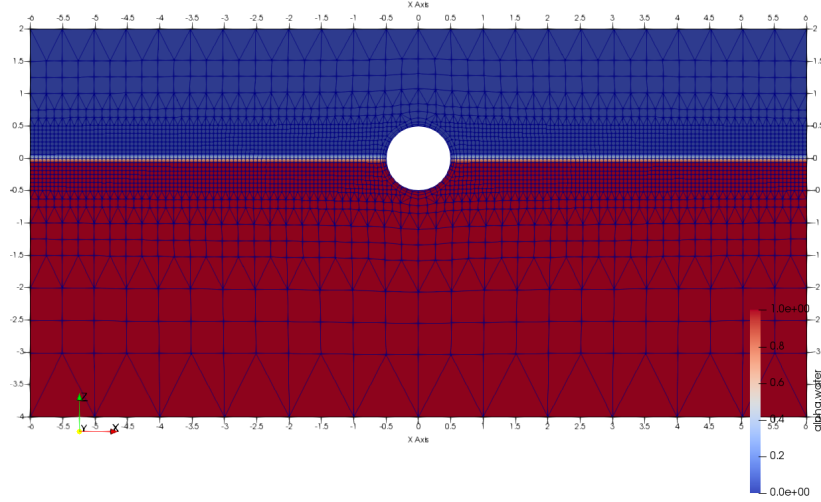
Figure 4.11: Cylinder in a coarse mesh with snapping, added layers and refinement around the object and the water surface.

the cells near the water surface were 0.0625 m in both x- and z-direction (refer to Figure 4.11). Before these changes, the mesh had 2552 cells, with most cells, including those near the water surface, being 0.3 m in width and 0.15 m in height (refer to Figure 4.9).

The volume of the cylinder became more accurate as it only sinks by 12 mm and stabilises at approximately −7 mm. In contrast, previous cases showed rises of 50 mm to 180 mm in the first three cases and sinking of 350 mm in the case where the mesh around the cylinder surface was refined. The stable heave position can be determined from the hydrostatic balance. Rearranging Equation (3.3) yields:

$$\pi \frac{\rho_c - \rho_w}{\rho_a - \rho_w} = \arccos\left(-h'\right) + h'\sqrt{1 - h'^2}. \tag{4.2}$$

where ρ_c is the density of the cylinder ($500 \, \text{kg m}^{-3}$), ρ_a is the density of air ($1 \, \text{kg m}^{-3}$), ρ_w is the density of water ($998.2 \, \text{kg m}^{-3}$). The resulting value of $h = rh' = h'$ is -0.63 mm, which is still over ten times less than the previous estimation.

4.4 Fully submerged cylinder heave in still water

The previous section analysed the stability and accuracy of a near-balanced cylinder. This section compares the experimental data presented in Section 3.2 with the simulation results. The floating object remains a cylinder. However, the dimensions are significantly reduced. According to the experiment's documentation, the diameter of the cylinder is 59 mm, the length is 243 mm, and the mass is 621 g. The analysis performed in Section 3.2 showed inconsistency in the data.
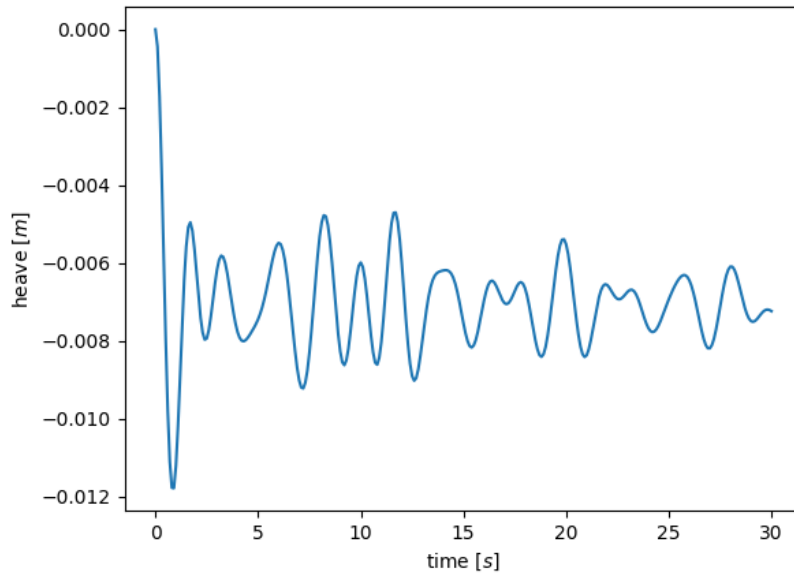
Figure 4.12: Heave time series for half-submerged cylinder in a coarse grid with local refinements around the object and the water surface over 30 s.

For this reason, two cylinders are considered. One is based on the documentation length, and the other keeps the other dimensions, adjusting the length to achieve the derived density of $898.49\,\mathrm{kg\,m^{-3}}$. The resulting length is $251.63\,\mathrm{m}$.

The new domain is adjusted to the much smaller dimensions of the cylinder. The tank is set to be $1\,\mathrm{m}$ long, $0.5\,\mathrm{m}$ in height and $243\,\mathrm{mm}$ in width. The water level is set to $205\,\mathrm{mm}$. The simulations concern only the first three seconds. Thus there is no need for a long tank, as the wave reflections do not influence the heave noticeably. The grading of the mesh is set in most cases to 64 in length, 32 in height and 1 in width, thus keeping the two-dimensional domain. The cylinder's mesh is the file `smallCylinder.stl` for the nominal size cylinder, and in the file `expandedSmallCylinder.stl` for the longer cylinder.

The simulations are split into two groups, one for each cylinder length.

Documentation based length

There were four domain meshes used for this group. All of them used three areas of refinement. Refinement surface of the cylinder, a box surrounding the cylinder spanning $-0.1\,\mathrm{m}$ to $0.1\,\mathrm{m}$ in length and $-0.08\,\mathrm{m}$ to $0.02\,\mathrm{m}$ in height and a water level box spanning the entire length of the tank and $-5\,\mathrm{mm}$ to $5\,\mathrm{mm}$ in height. The refinement levels for each mesh were as follows:

1. Mesh 'A' - 32x64x1, refinement level set to 4 for each refinement region. The volume of the floating object is $6.6266 \times 10^{-4}\,\mathrm{m^3}$ or 0.9974 of the nominal volume. The density of the cylinder is $937.13\,\mathrm{kg\,m^{-3}}$, and the equilibrium heave position is $6.5785\,\mathrm{mm}$.

2. Mesh 'B' - 128x256x1, refinement level set to 4 for each refinement region. The volume of the floating object is $6.6285 \times 10^{-4}\,\mathrm{m}^3$, or 0.9977 of the nominal volume. Density of the cylinder is $936.86\,\mathrm{kg\,m}^{-3}$, and the equilibrium heave position is $6.5992\,\mathrm{mm}$.

3. Mesh 'C' - 32x64x1, refinement level set to 2 for both box regions and 7 for the cylinder's surface with three layers added around. The volume of the floating object is $6.6286 \times 10^{-4}\,\mathrm{m}^3$, or 0.9977 of the nominal volume. The density of the cylinder is $936.85\,\mathrm{kg\,m}^{-3}$, and the equilibrium heave position is $6.5992\,\mathrm{mm}$.

4. Mesh 'D' - 32x64x1, refinement level set to 5 for each refinement region, three layers added around the cylinder. The volume of the floating object is $6.6282 \times 10^{-4}\,\mathrm{m}^3$, or 0.9977 of the nominal volume. Density of the cylinder is $936.91\,\mathrm{kg\,m}^{-3}$ and the equilibrium heave position is $6.5962\,\mathrm{mm}$.

All run cases used the k-epsilon turbulence model. Because of the initial static state of the simulation, the turbulent kinetic energy should be equal to zero. As that would lead to singularities when doing divisions, and because of no possibility to fully terminate any water movement in the experimental cases, both k and ϵ are set to a low, non-zero value. According to Online 2014

$$k = \frac{3}{2}\left(UI\right)^2, \tag{4.3}$$

$$\epsilon = C_\mu \frac{k^{\frac{3}{2}}}{l}, \tag{4.4}$$

where U is the mean flow velocity (equal to 0), I is the turbulence intensity (according to Online 2022, $1\,\%$ to $5\,\%$ for medium-turbulence cases and below 1% for low-turbulence cases), C_μ is the turbulence model constant, usually set to 0.09, and l is the turbulent length scale or the size of the large energy-containing eddies. For the first set of runs, both k and ϵ were set to 0.001, and both I and l were set to 0.01.

The following nine simulation runs were performed:

Run 1

The first run case used the same configurations as the original *floating object* tutorial, except for the time scheme, which is still set to Crank-Nicolson, although with a lower coefficient. This value follows the conclusions of the previous section and is the same choice as in Kramer et al. 2021. Because of mesh inaccuracies, the volume of the cylinder is not equal to the nominal. Thus, the density is slightly higher. The difference is minuscule enough that the impact should not be noticeable in any way.

The entire configuration is shown in Table 4.1. The inner and outer distances are set to 0.05 and 0.1, respectively. These values are a good balance between the stability of the simulation, its accuracy and computation time. It is advisable to perform additional tests with different values.

Figure 4.13 depicts the heave time series for run case 1. There was a sudden singularity at approximately $1.15\,\mathrm{s}$, possibly caused by the maximum Courant number frequently exceeding 1 (see Figure 4.14). In order to prevent

mesh		D
inner warping distance		0.05
outer warping distance		0.1
schemes		
time	default	CrankNicolson 0.5
gradient	default	Gauss linear
divergence	default	linear
	(rhoPhi,U)	Gauss vanLeerV
	(phi,alpha)	Gauss interfaceCompression vanLeer 1
	(phi,k)	Gauss upwind
	(phi,epsilon)	Gauss upwind
Laplacian	default	Gauss linear corrected
interpolation	default	linear
surface normal gradient	default	corrected
PIMPLE		
momentum predictor		no
outer correctors		3
correctors		1
non-orthogonal correctors		0
correct phi		yes
move mesh outer corrector		yes
control		
maximum Courant number		1
maximum alpha Courant number		1

Table 4.1: Settings for the run 1.
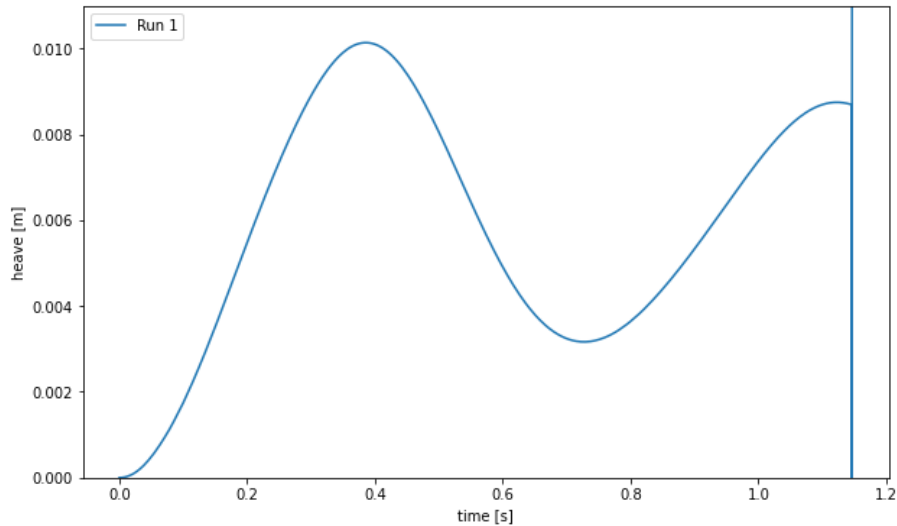
Figure 4.13: Heave time series for run case 1.
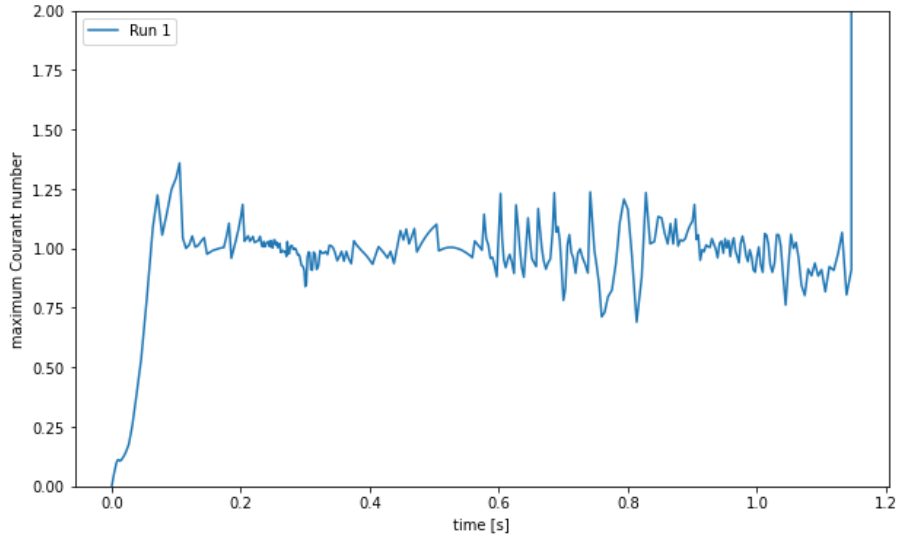
Figure 4.14: Maximum Courant number time series for run case 1.

mesh	D
inner warping distance	0.05
outer warping distance	0.1
schemes as in Table 4.1	
PIMPLE as in Table 4.1	
control	
maximum Courant number	0.5
maximum alpha Courant number	0.5

Table 4.2: Settings for the run 2.

a recurrence of this scenario, a new limit of 0.5 has been established for all upcoming cases involving running.

Run 2

As shown in Figure 4.15, limiting the Courant number lowers the values significantly. Still, rising visibly above the limit, the Courant Number for the second run case does not approach 1, and its maximum value is less than 0.7. Figure 4.17 illustrates the heave of the cylinder in the second run case.

The simulation of run case 2 performed 6960 PIMPLE iterations, taking 1313 s.

Run 3

According to Guerrero 2022, PIMPLE should use a minimum of two outer correctors for moving bodies, at least three outer correctors in general cases (4 for highly transient flows or strongly coupled problems) and at least one non-orthogonal corrector (more in case bad quality meshes or when large mesh deformation occurs). Moreover, the momentum predictor is suggested to be set
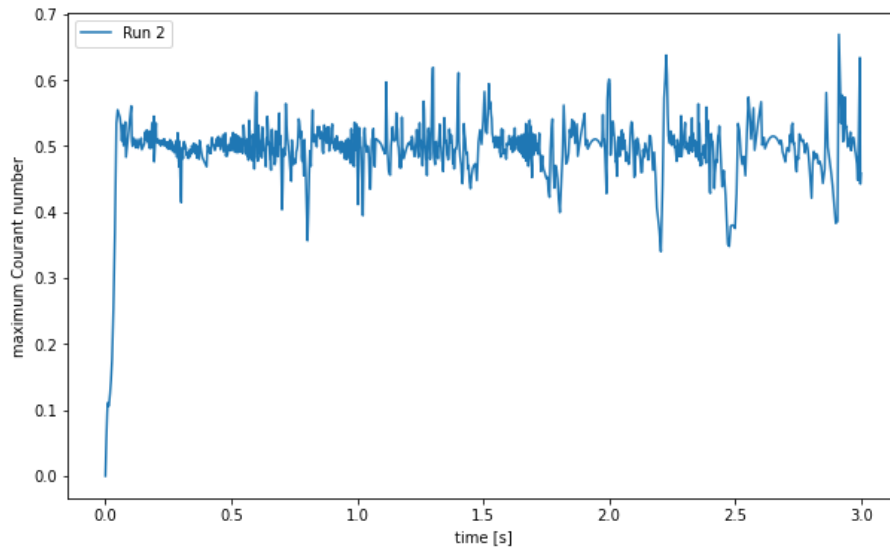
Figure 4.15: Maximum Courant number for run case 2.
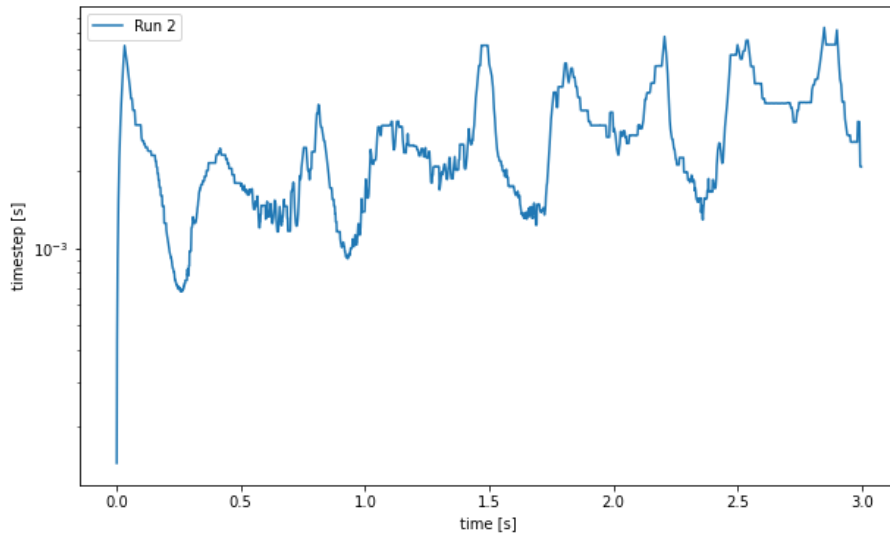
Figure 4.16: Time steps for run case 2.
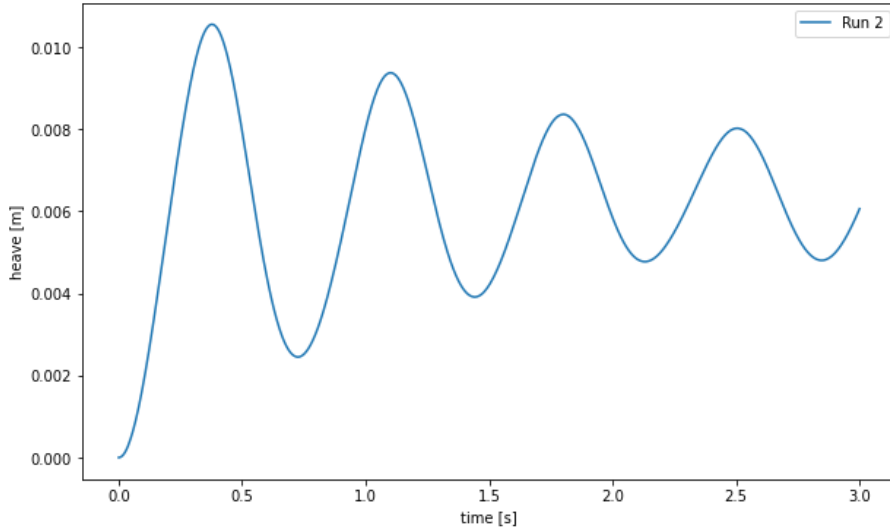
Figure 4.17: Heave time series for run case 2.

mesh	D
inner warping distance	0.05
outer warping distance	0.1
schemes as in Table 4.1	
PIMPLE	
momentum predictor	yes
outer correctors	2
correctors	3
non-orthogonal correctors	1
correct phi	yes
move mesh outer corrector	yes
control as in Table 4.2	

Table 4.3: Settings for the run 3.

on. The third case run's configuration expands on the second case by including the above-mentioned suggestions.

In the third run case, Figures 4.18 and 4.19 show less damping and a slight increase in frequency. Even though there are higher amplitudes and velocities, the Courant number is generally lower, resulting in longer time steps (see Figure 4.20).

The simulation of run case 3 performed 6605 PIMPLE iterations, taking 1160 s.

Run 4

The last alteration based on Guerrero 2022 is setting the gradient scheme for the velocity field to cellLimited Gauss linear with coefficient set to 1, the divergence scheme for (rhoPhi,U) to Gauss linearUpwind concerning the velocity gradient, and the divergence scheme for (phi,alpha) to Gauss vanLeer.
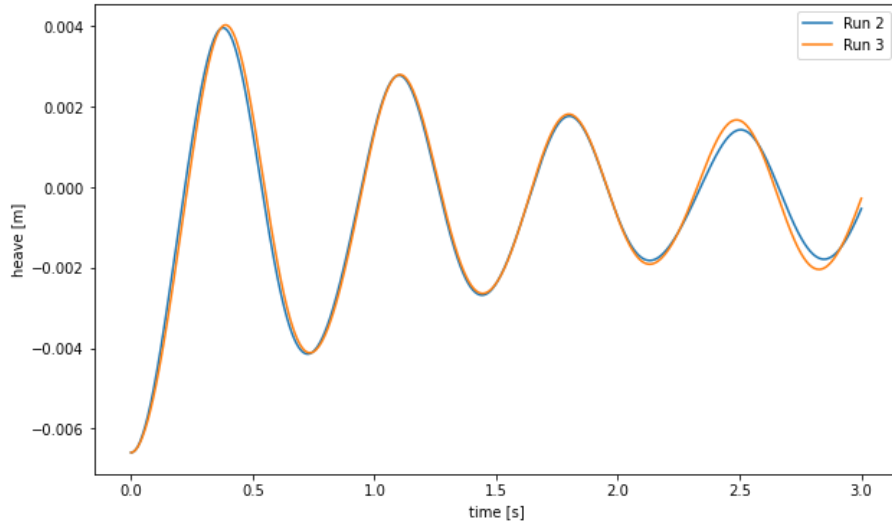
Figure 4.18: Heave time series comparison between run cases 2 and 3.
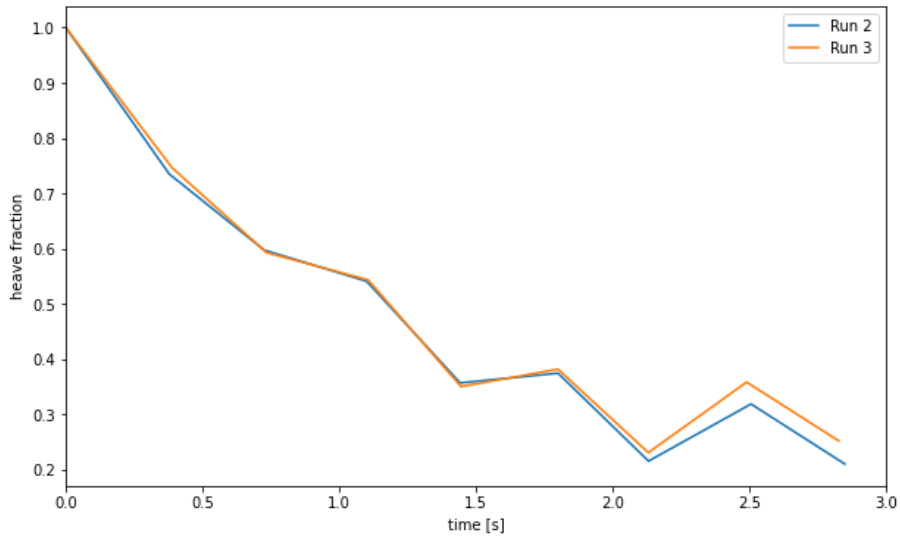
Figure 4.19: Amplitude decay comparison between run cases 2 and 3.
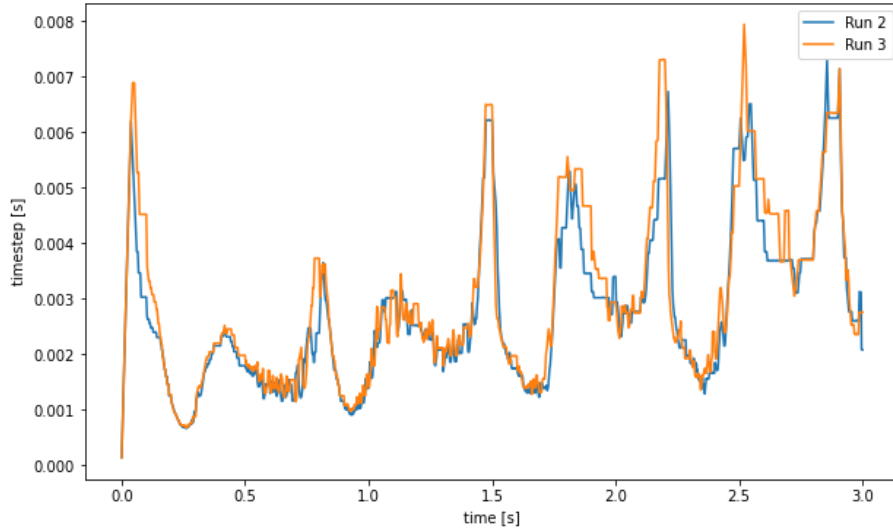
Figure 4.20: Time steps length comparison between run cases 2 and 3.

mesh		D
inner warping distance		0.05
outer warping distance		0.1
schemes differences from Table 4.1		
gradient	(U)	cellLimited Gauss linear 1
divergence	(rhoPhi,U) (phi,alpha)	Gauss linearUpwindV grad(U) Gauss vanLeer
Laplacian	default	Gauss linear limited 1
surface normal gradient	default	limited 1
PIMPLE as in Table 4.3		
control as in Table 4.2		

Table 4.4: Settings for the run 4.

Gauss gradient schemes calculate gradient values using Gauss' theorem

$$\int_V (\nabla \cdot \vec{u}) \ dV = \oint_S (\vec{n} \cdot \vec{u}) \ dS. \tag{4.5}$$

According to The OpenFOAM Foundation Ltd 2011–2023, the cell gradient is limited to ensure that the face values obtained by extrapolating the cell value to the cell faces using the gradient are bounded by the neighbouring cells minimum and maximum limits. A linear upwind scheme is a second order, upwind interpolation scheme with an explicit correction based on the local cell gradient. The V variant calculates a single limiter applied to all components of the vector based on the direction of most rapidly changing gradient. Van Leer scheme is an unbounded, second order scheme. Finally, limited is chosen for both the Laplacian (linear) and the surface normal gradient schemes.

mesh	A
inner warping distance	0.05
outer warping distance	0.1
schemes as in Table 4.4	
PIMPLE as in Table 4.3	
control as in Table 4.2	

Table 4.5: Settings for the run 5.
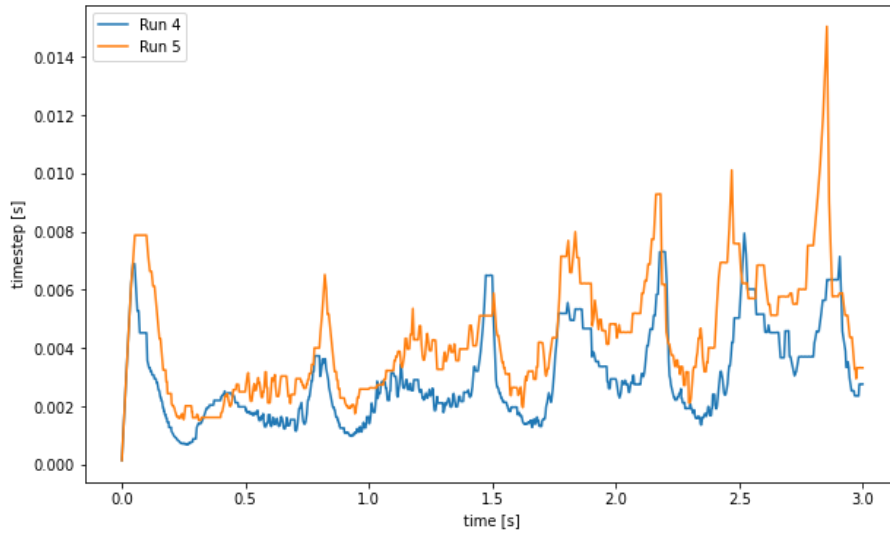
Figure 4.21: Time step length comparison between run cases 4 and 5.

The simulation of run case 3 performed 6605 PIMPLE iterations, taking 1118 s.

Run 5

In all previous test cases, mesh 'D' was utilised. However, three additional test cases were conducted to comprehend the mesh refinement effects better. The first test case implemented mesh 'A', which had the same initial grading as mesh 'D', but was refined one level less in all areas. Even though it had a higher density, this fifth test case experienced less drag (see Figure 4.22), resulting in slower amplitude damping and higher frequency. Because of the coarser grid, time steps were longer, which expedited the simulation process (see Figure 4.21).

The simulation of run case 5 performed 4235 PIMPLE iterations, taking 268 s.

Run 6

Another test was conducted on mesh 'B' to observe the impact of further refinement. Similar to the previous test, it was discovered that the mesh refinement led to increased drag and slower execution. The former could be

mesh	B
inner warping distance	0.05
outer warping distance	0.1
schemes as in Table 4.5	
PIMPLE as in Table 4.3	
control as in Table 4.2	

Table 4.6: Settings for the run 6.

mesh	C
inner warping distance	0.05
outer warping distance	0.1
schemes as in Table 4.5	
PIMPLE as in Table 4.3	
control as in Table 4.2	

Table 4.7: Settings for the run 7.
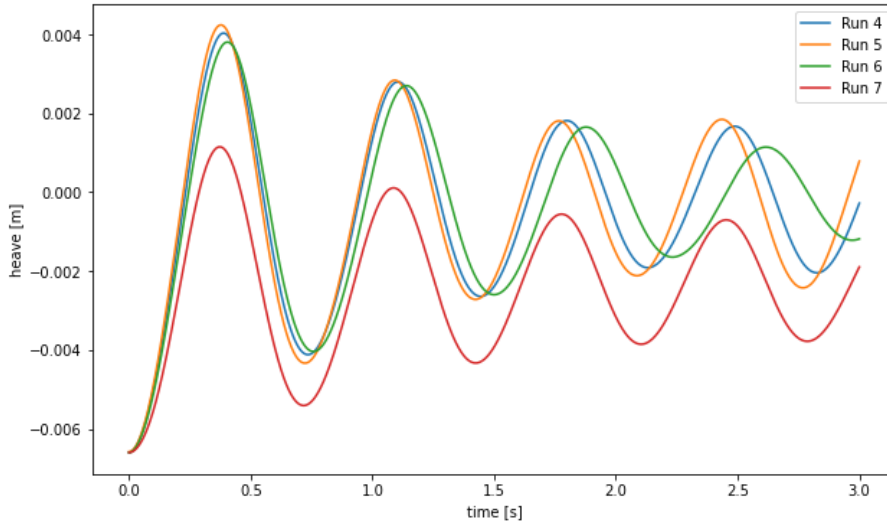
Figure 4.22: Heave time series comparison between run cases 4, 5, 6 and 7.

attributed to the turbulence properties that are more pronounced with smaller cell sizes.

The simulation of run case 6 performed 14685 PIMPLE iterations, taking 11 789 s.

Run 7

The previous meshes refined the cylinder surrounding and the water level with the same level. Another option is to refine only the cylinder and slightly improve the mesh quality in the area of water-air phase change. Mesh 'C' was refined seven times around the floating object and only twice around the water level.

As a result of the inferior quality of the mesh around the water level, despite the density being nearly identical, the heave dampens much faster and stabilises

mesh	D
inner warping distance	0.05
outer warping distance	0.1
schemes differences from Table 4.5	

time	default	CrankNicolson 0.9
PIMPLE as in Table 4.3		
control as in Table 4.2		

Table 4.8: Settings for the run 8.
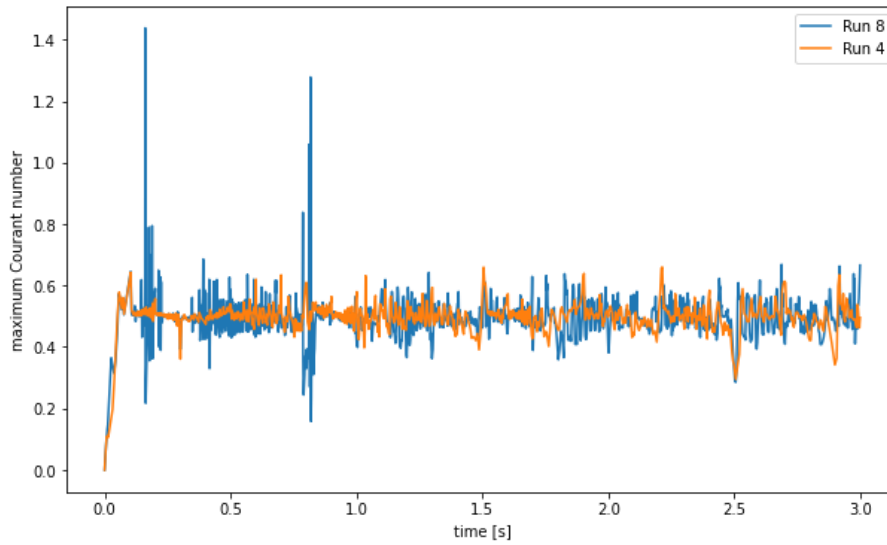
Figure 4.23: Maximum Courant number comparison for run cases 4 and 8.

at a lower elevation. This outcome illustrates the importance of keeping the water level simulated adequately across the domain.

The simulation of run case 7 performed 25525 PIMPLE iterations, taking 688 s.

Run 8

The final test case for the cylinder of standard length involved examining the behaviour for a higher coefficient of the Crank-Nicolson time scheme, which was set to 0.9. When set to 1, the simulation quickly diverged and led to singularities. The Courant number exceeded 1 several times (as seen in Figure 4.23), which made the results less reliable. One solution could be to lower the limit of the Courant number. The maximum jump was almost 1.5, so it may be advisable to lower the limit by at least 0.3.

The simulation of run case 8 performed 28990 PIMPLE iterations, taking 8215 s.

mesh	E
inner warping distance	0.05
outer warping distance	0.1
turbulence model	k-epsilon
surface tension	none
k	$0.001\,\mathrm{m^2\,s^{-2}}$
ϵ	$0.001\,\mathrm{m^2\,s^{-3}}$
turbulence intensity	0.01
turbulence length scale	0.01
rigid body acceleration relaxation	0.7
schemes as in Table 4.5	
PIMPLE as in Table 4.3	
control	
maximum Courant number	0.2
maximum alpha Courant number	0.2

Table 4.9: Settings for the run 9.

Longer cylinder

Only one mesh, labelled as 'E', was utilised in this section. Its dimensions are 1.5 m in length, 0.5 m in height and 0.251 63 m in width. The grading is 96 in length, 32 in height and 1 in width. Refinement regions are the same as in the previous cases, with the refinement level set for each of them to 5. The length of the tank was adjusted to the tank's dimensions used for the experiments. The resulting density is $891.67\,\mathrm{kg\,m^{-3}}$, and the equilibrium heave position is 9.6642 mm.

Unlike the nominal-length cylinder run cases, the cases below include various turbulence models. Four turbulence models were considered:

- k-ϵ - a well-studied model that is very easy to implement. However, it is not well suited for low-Reynolds flows.

- k-ω - easy to implement and computationally efficient. May over-predict turbulence, leading to overdamping.

- Shear Stress Transport k-ω - complex and sensitive to numerical errors. Accurate at near-wall treatment and good prediction of free shear stress. Well suited for low-Reynolds flows.

- Laminar - no turbulence model.

The initial setup did not include the surface tension effects. Because of small size of the cylinder, impact of the surface tension is significant. Thus, all the turbulence models are tested with and without the surface tension.

The following simulations were performed:
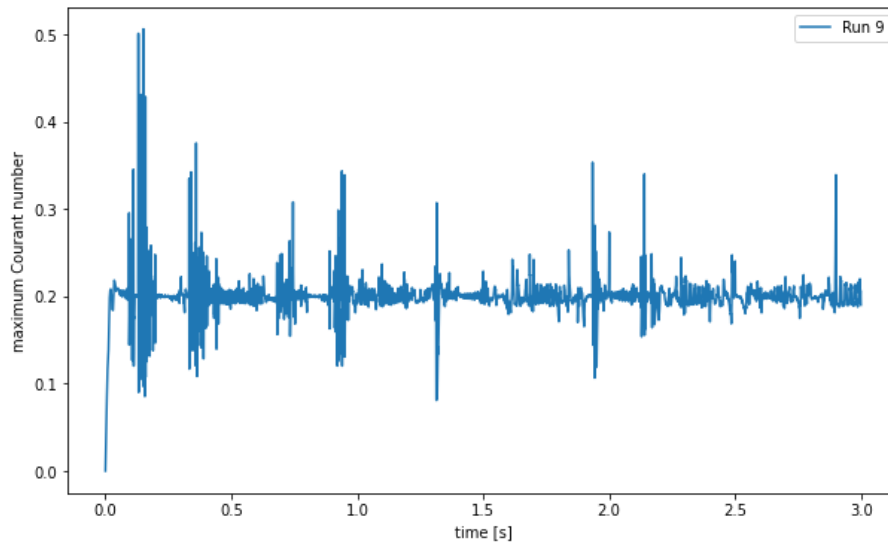
Figure 4.24: Maximum Courant number for run case 9.

Run 9

The ninth run case utilises the same configuration settings as the fourth one. The only change made was using a wider mesh, specifically mesh 'E'. This makes the cylinder less dense and compliant with the experimental results. This and the succeeding run cases analyse the cylinder damping due to energy losses. There are four mechanisms of energy loss in the simulation: wave radiation, turbulent dissipation, over-relaxation and numerical errors.

Initial tests for maximum Courant number set to 0.5 yielded several peaks, when the Courant number rose above 2.5. To avoid possible accuracy loss, the upper limit was set to 0.2. Figure 4.24 presents several peaks of the Courant number barely reaching above 0.5.

The simulation of run case 9 performed 9990 PIMPLE iterations, taking 2706 s.

Run 10

A standard temperature of $20\,^\circ$C and air pressure of $101.3\,$kPa were chosen. According to Surface Tension 2017, the surface tension on a water-air interface for these parameters is $0.0728\,$N m^{-1}. Maximum Courant number rose up over 0.7 (refer to Figure 4.25), still within the safe limit of 1.

The simulation of run case 10 performed 64975 PIMPLE iterations, taking 17 113 s.

Run 11

To analyse the impact of higher Courant number limit, run case 11 was performed with the limit set to 0.5. As seen in Figure 4.26, the maximum Courant number rose over 6, far beyond the values for the previous run cases (see Figure 4.28). Such high values usually make the results unreliable. However, Figure 4.29

mesh	E
inner warping distance	0.05
outer warping distance	0.1
turbulence model	k-epsilon
surface tension	$0.0728\,\mathrm{N\,m^{-1}}$
k	$0.001\,\mathrm{m^2\,s^{-2}}$
ϵ	$0.001\,\mathrm{m^2\,s^{-3}}$
turbulence intensity	0.01
turbulence length scale	0.01
rigid body acceleration relaxation	0.7
schemes as in Table 4.5	
PIMPLE as in Table 4.3	
control as in Table 4.9	

Table 4.10: Settings for the run 10.
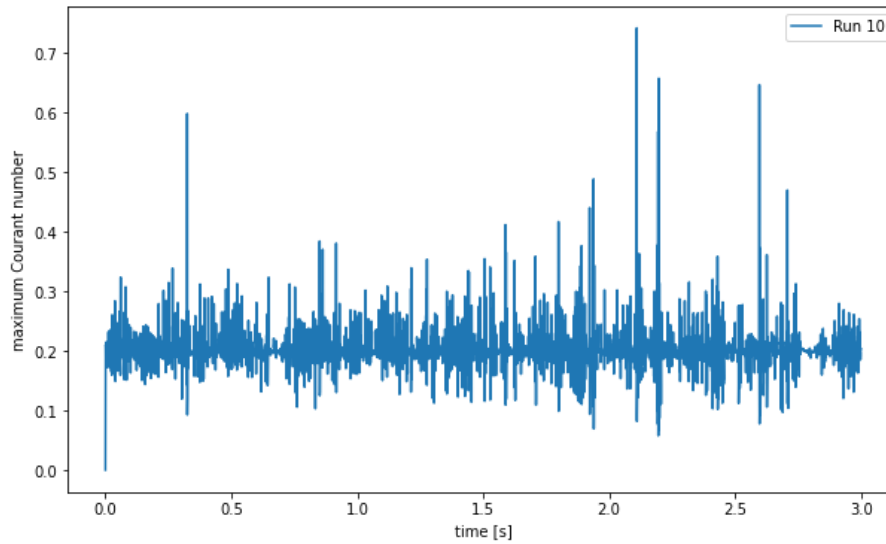
Figure 4.25: Maximum Courant number for run case 10.

mesh	E
inner warping distance	0.05
outer warping distance	0.1
turbulence model	k-epsilon
surface tension	$0.0728\,\mathrm{N\,m^{-1}}$
k	$0.001\,\mathrm{m^2\,s^{-2}}$
ϵ	$0.001\,\mathrm{m^2\,s^{-3}}$
turbulence intensity	0.01
turbulence length scale	0.01
rigid body acceleration relaxation	0.7
schemes as in Table 4.5	
PIMPLE as in Table 4.3	
control	
maximum Courant number	0.5
maximum alpha Courant number	0.5

Table 4.11: Settings for the run 11.
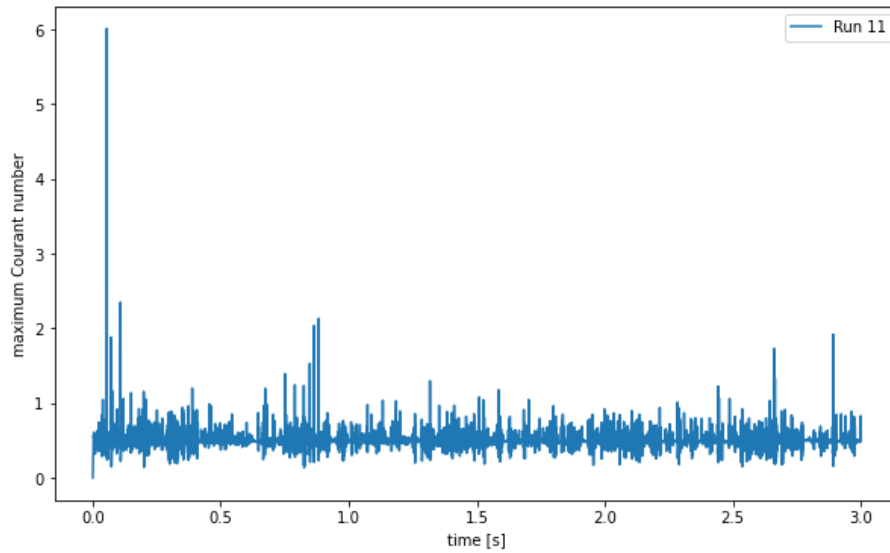
Figure 4.26: Maximum Courant number for run case 11.
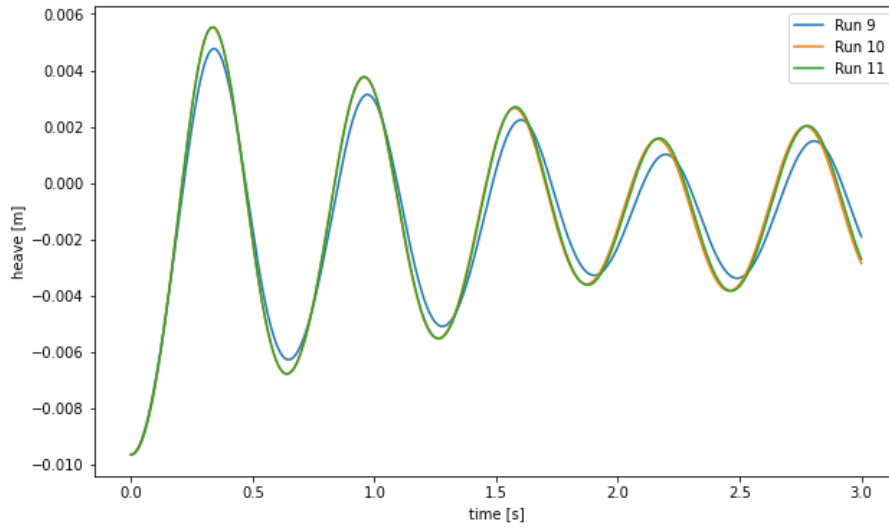
Figure 4.27: Heave time series comparison for run cases 9, 10 and 11.
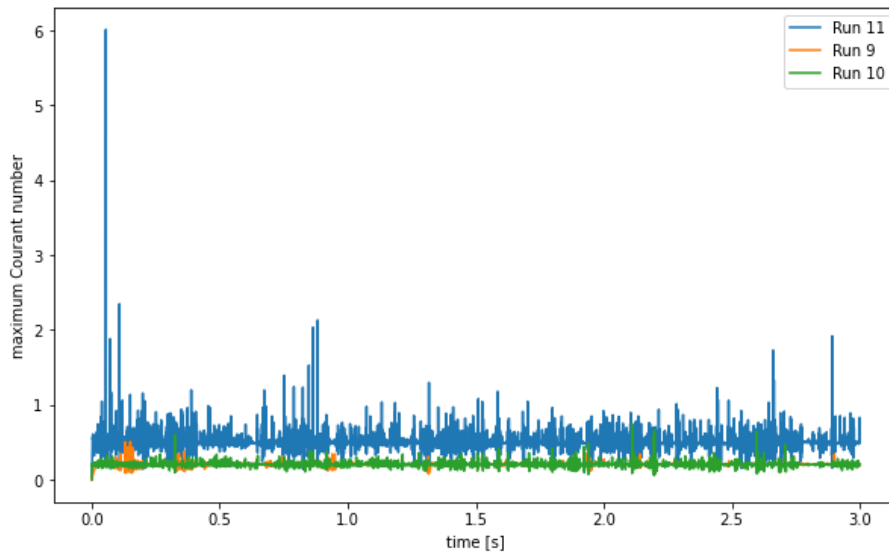
Figure 4.28: Maximum Courant number comparison for run cases 9, 10 and 11.
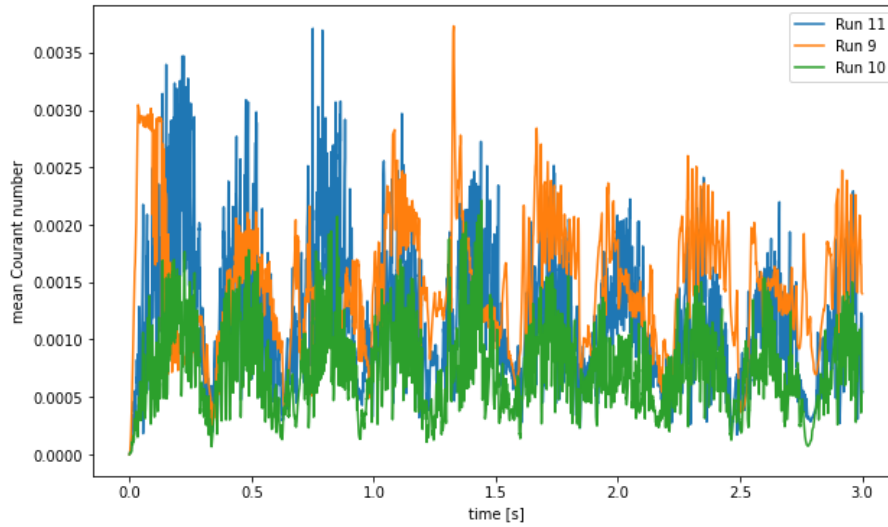
Figure 4.29: Mean Courant number comparison for run cases 9, 10 and 11.

illustrates, that the mean Courant number value did not stand significantly out from the previous two cases. The low levels 0.001 to 0.0035 mean, that the huge exceeding was just a local anomaly with little impact on the general result of the simulation.

Figure 4.27 compares the heave time series for run cases 9, 10 and 11. Little to no divergence seem to occur between run cases 10 and 11. The minuscule difference in the end may result more from the time step length difference than from the initial anomaly. Run case 9 stops its rise much lower, showing the significant impact of the surface tension.

The simulation of run case 11 performed 37475 PIMPLE iterations, taking 9983 s.

Run 12

Run case 12 utilised another turbulence model, k-ω. Instead of solving for the dissipation rate of turbulent kinetic energy (ϵ), this model solves for the specific dissipation rate. Online 2014; Wilcox et al. 1998 state that the internal field's initial specific turbulent dissipation rate can be computed as $\omega = \frac{\sqrt{k}}{l}$. Again, that may lead to singularities. Thus, an arbitrarily small value has been chosen for the initial ω.

Similarly to the k-ϵ cases, three simulation runs were performed. Run case 12 with no surface tension, run case 13 with surface tension and low Courant number cap of 0.2, and run case 14 with surface tension and high Courant number cap of 0.5.

The simulation of run case 12 performed 30880 PIMPLE iterations, taking 9296 s.

| mesh	E
inner warping distance	0.05
outer warping distance	0.1
turbulence model	k-omega
surface tension	none
k	$0.001\,\mathrm{m^2\,s^{-2}}$
ω	$0.001\,\mathrm{s^{-1}}$
turbulence intensity	0.01
turbulence length scale	0.01
rigid body acceleration relaxation	0.7
schemes as in Table 4.5	
PIMPLE as in Table 4.3	
control as in Table 4.9	

Table 4.12: Settings for the run 12.

mesh	E
inner warping distance	0.05
outer warping distance	0.1
turbulence model	k-omega
surface tension	$0.0728\,\mathrm{N\,m^{-1}}$
k	$0.001\,\mathrm{m^2\,s^{-2}}$
ω	$0.001\,\mathrm{s^{-1}}$
turbulence intensity	0.01
turbulence length scale	0.01
rigid body acceleration relaxation	0.7
schemes as in Table 4.5	
PIMPLE as in Table 4.3	
control as in Table 4.9	

Table 4.13: Settings for the run 13.

Run 13

Run case 13 expanded on the previous case by adding surface tension. The configuration is given in Table 4.13.

The simulation of run case 13 performed 60545 PIMPLE iterations, taking $18\,207\,\mathrm{s}$.

Run 14

Comparing to Figure 4.27, heave time series for different maximum Courant number are differing much more visibly in run cases 13 and 14 (see Figure 4.30. The Courant number did not reach as high values. Still, it rose above 3 and was reaching 1 multiple times. Interestingly, mean Courant number values were much lower for k-ω cases (see Figure 4.32) then those for k-ϵ.

The simulation of run case 14 performed 33640 PIMPLE iterations, taking $9870\,\mathrm{s}$.

mesh	E
inner warping distance	0.05
outer warping distance	0.1
turbulence model	k-omega
surface tension	$0.0728 \, \mathrm{N \, m^{-1}}$
k	$0.001 \, \mathrm{m^2 \, s^{-2}}$
ω	$0.001 \, \mathrm{s^{-1}}$
turbulence intensity	0.01
turbulence length scale	0.01
rigid body acceleration relaxation	0.7
schemes as in Table 4.5	
PIMPLE as in Table 4.3	
control	
maximum Courant number	0.5
maximum alpha Courant number	0.5

Table 4.14: Settings for the run 14.
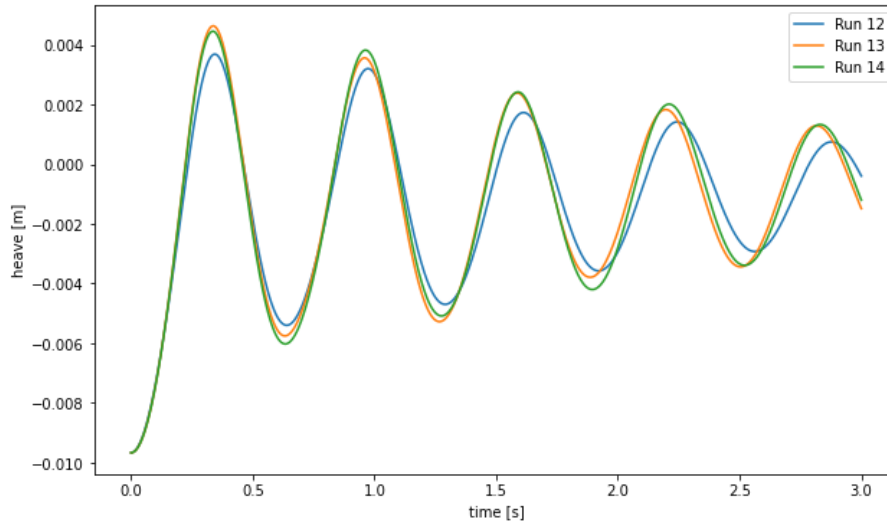

Figure 4.30: Heave time series comparison between run cases 12, 13 and 14.
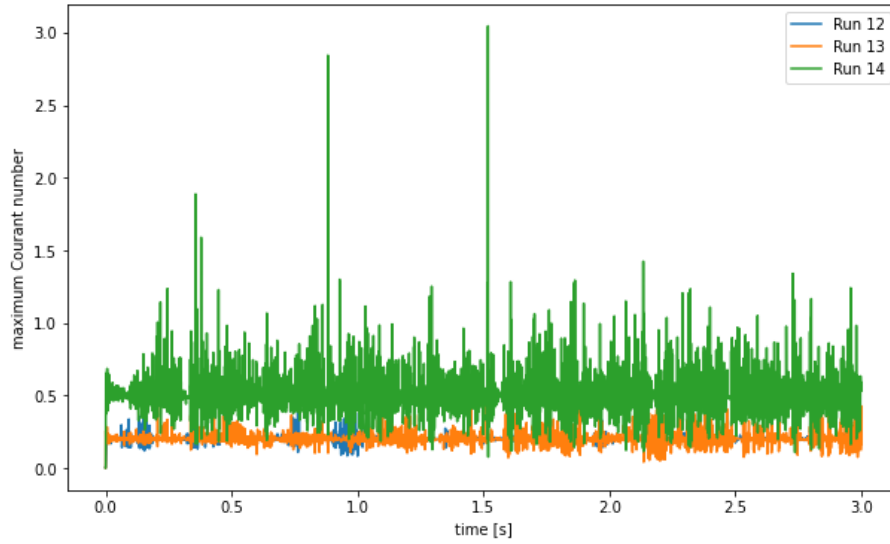
Figure 4.31: Maximum Courant number comparison between run cases 12, 13 and 14.
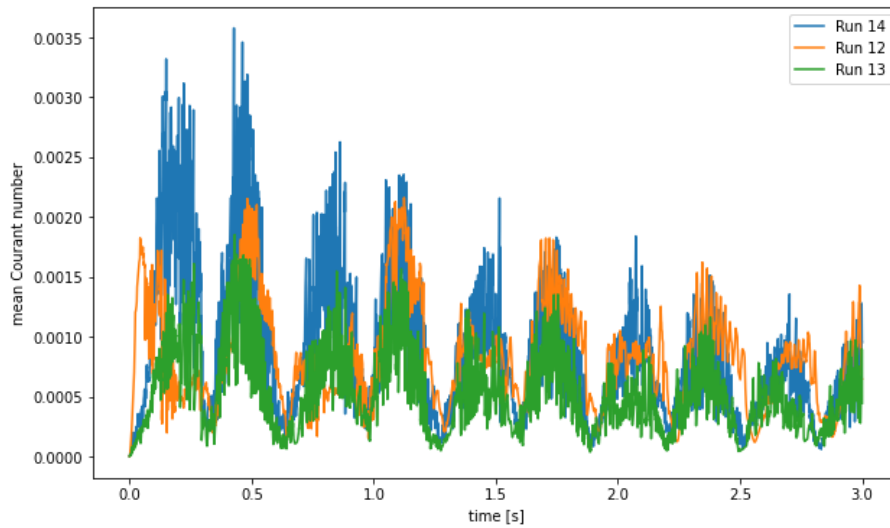
Figure 4.32: Mean Courant number comparison between run cases 12, 13 and 14.

mesh	E
inner warping distance	0.05
outer warping distance	0.1
turbulence model	k-omega SST
surface tension	none
k	$0.001\,\mathrm{m^2\,s^{-2}}$
ω	$0.001\,\mathrm{s^{-1}}$
turbulence intensity	0.01
turbulence length scale	0.01
rigid body acceleration relaxation	0.7
schemes as in Table 4.5	
PIMPLE as in Table 4.3	
control as in Table 4.9	

Table 4.15: Settings for the run 15.

Run 15

Menter, Kuntz and Langtry 2003 introduced their Shear Stress Transport variant as an improvement to the standard k-ω model. Instead of calculating the turbulent viscosity from both k and ω fields, k-ω SST utilises only the ω field and applies a correction function incorporating the distance to the nearest wall, the magnitude of the strain rate tensor, and the ratio of turbulent to molecular viscosity. Thanks to that, k-ω SST is much better at handling adverse pressure gradients and is more accurate at predicting the near-wall region state. Both of these are critical points of the simulations performed within the scope of this paper.

Among the simulations discussed by Kramer et al. 2021, five were performed in OpenFOAM: three with no turbulence model, and two using k-ω SST. Those were, however, performed on a spherical buoy, with a much farther initial location from the equilibrium point ($H = 0.5D$).

The simulation of run case 15 performed 29735 PIMPLE iterations, taking $9718\,\mathrm{s}$.

Run 16

The configurations for run case 16 are shown in Table 4.16. The simulation performed 84635 PIMPLE iterations, taking $29\,839\,\mathrm{s}$.

Run 17

The configuration for run case 17 is displayed in Table 4.17. Figure 4.33 illustrates the difference between the cases with and the case without surface tensions effects. Moreover, Figures 4.34 and 4.35 display maximum and mean Courant number comparison between the run cases. Despite smaller heave, no surface tension effects and lower Courant number cap, run case 15 dominates the mean Courant number values throughout most of the simulation.

The simulation of run case 17 performed 46050 PIMPLE iterations, taking $15\,237\,\mathrm{s}$.
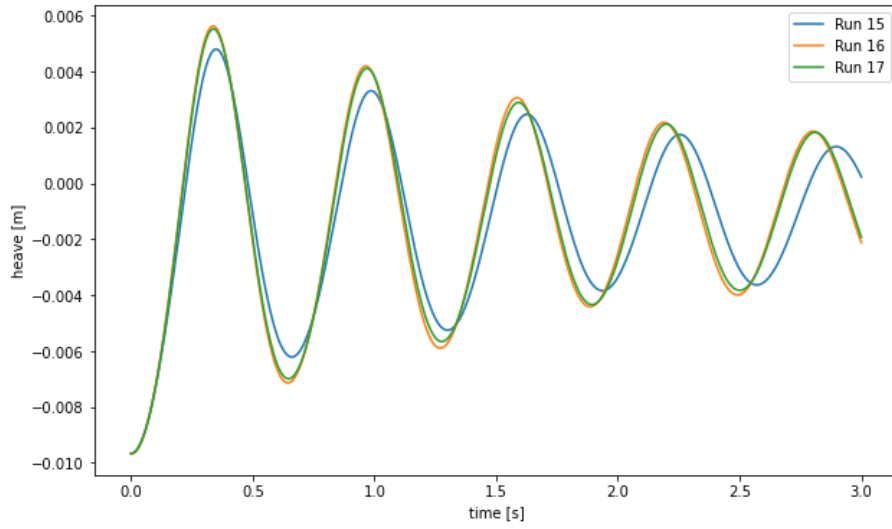
Figure 4.33: Heave time series comparison between run cases 15, 16 and 17.
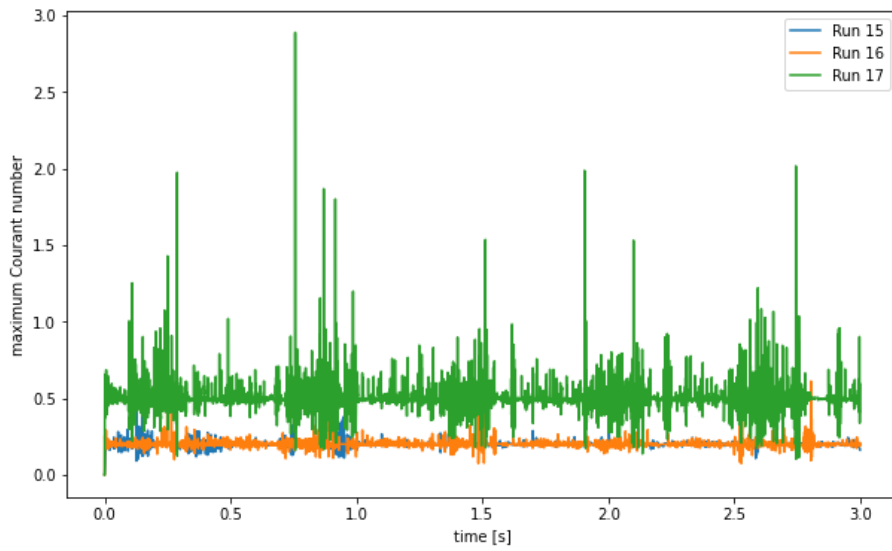
Figure 4.34: Maximum Courant number comparison between run cases 15, 16 and 17.

mesh	E
inner warping distance	0.05
outer warping distance	0.1
turbulence model	k-omega SST
surface tension	$0.0728\,\mathrm{N\,m^{-1}}$
k	$0.001\,\mathrm{m^2\,s^{-2}}$
ω	$0.001\,\mathrm{s^{-1}}$
turbulence intensity	0.01
turbulence length scale	0.01
rigid body acceleration relaxation	0.7
schemes as in Table 4.5	
PIMPLE as in Table 4.3	
control as in Table 4.9	

Table 4.16: Settings for the run 16.

mesh	E
inner warping distance	0.05
outer warping distance	0.1
turbulence model	k-omega SST
surface tension	$0.0728\,\mathrm{N\,m^{-1}}$
k	$0.001\,\mathrm{m^2\,s^{-2}}$
ω	$0.001\,\mathrm{s^{-1}}$
turbulence intensity	0.01
turbulence length scale	0.01
rigid body acceleration relaxation	0.7
schemes as in Table 4.5	
PIMPLE as in Table 4.3	
control	
maximum Courant number	0.5
maximum alpha Courant number	0.5

Table 4.17: Settings for the run 17.

Run 18

Another run case set has been conducted to estimate the losses due to turbulent dissipation. The turbulence model was set to laminar to eliminate the impact of turbulence. Unlike run cases 9, 12 and 15, which also did not include surface tension, run case 18 used maximum Courant number cap of 0.5. There are two clear instabilities visible in Figure 4.36. The Courant number rose up to 2.5 potentially greatly impacting the simulation accuracy.

Simulation performed 45185 PIMPLE iterations, taking $11\,517\,\mathrm{s}$.

Run 19

Run case 19 utilised the same laminar model as run case 18. However, surface tension effects were included and the maximum Courant number cap was set
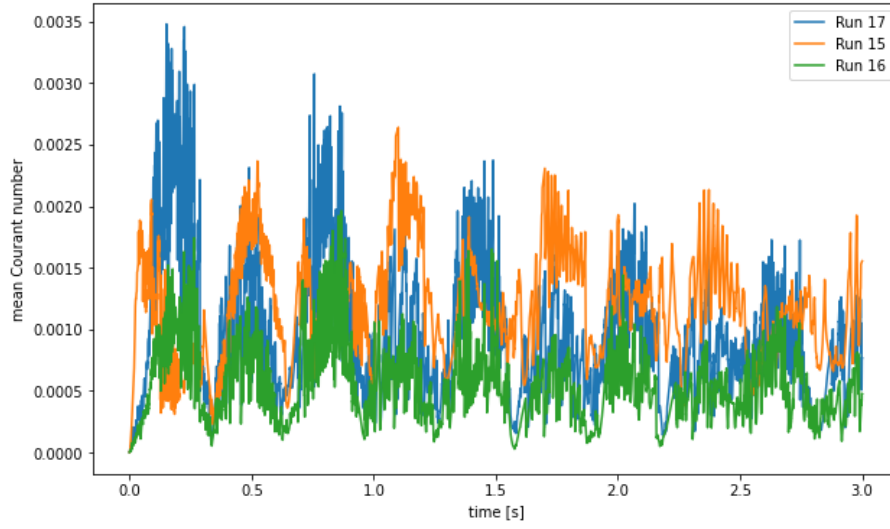
Figure 4.35: Mean Courant number comparison between run cases 15, 16 and 17.

mesh	E
inner warping distance	0.05
outer warping distance	0.1
turbulence model	laminar
surface tension	none
turbulence intensity	0.01
turbulence length scale	0.01
rigid body acceleration relaxation	0.7
schemes as in Table 4.5	
PIMPLE as in Table 4.3	
control as in Table 4.9	

Table 4.18: Settings for the run 18.

mesh	E
inner warping distance	0.05
outer warping distance	0.1
turbulence model	laminar
surface tension	$0.0728\,\mathrm{N\,m^{-1}}$
turbulence intensity	0.01
turbulence length scale	0.01
rigid body acceleration relaxation	0.7
schemes as in Table 4.5	
PIMPLE as in Table 4.3	
control as in Table 4.9	

Table 4.19: Settings for the run 19.
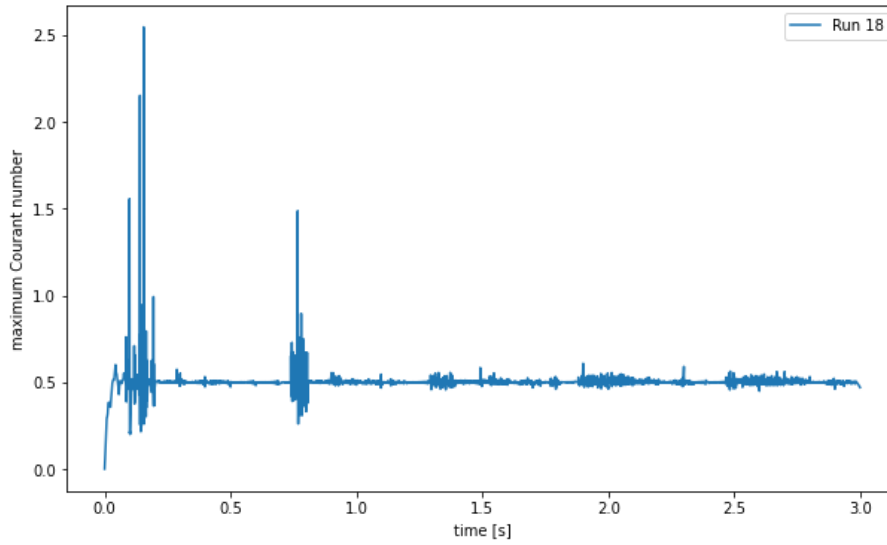
Figure 4.36: Maximum Courant number for run case 18.

mesh	E
inner warping distance	0.05
outer warping distance	0.1
turbulence model	laminar
surface tension	$0.0728\,\mathrm{N\,m^{-1}}$
turbulence intensity	0.01
turbulence length scale	0.01
rigid body acceleration relaxation	0.7
schemes as in Table 4.5	
PIMPLE as in Table 4.3	
control	
maximum Courant number	0.5
maximum alpha Courant number	0.5

Table 4.20: Settings for the run 20.

back to 0.2. The simulation performed 109665 PIMPLE iterations, taking $26\,709\,\mathrm{s}$.

Run 20

The last laminar run case used nearly the same configuration as run case 19. Only the Courant number was capped at 0.5 instead of 0.2. Figure 4.37 compares the heave time series between the laminar run cases and Figures 4.38 and 4.39 illustrate the maximum and mean Courant number across those. The simulation performed 55865 PIMPLE iterations, taking $13\,785\,\mathrm{s}$.

Further runs utilise the k-ω SST turbulence model. These runs were performed to analyse the sensitivity to parameter tuning.

Figure 4.37: Heave time series comparison between run cases 18, 19 and 20.

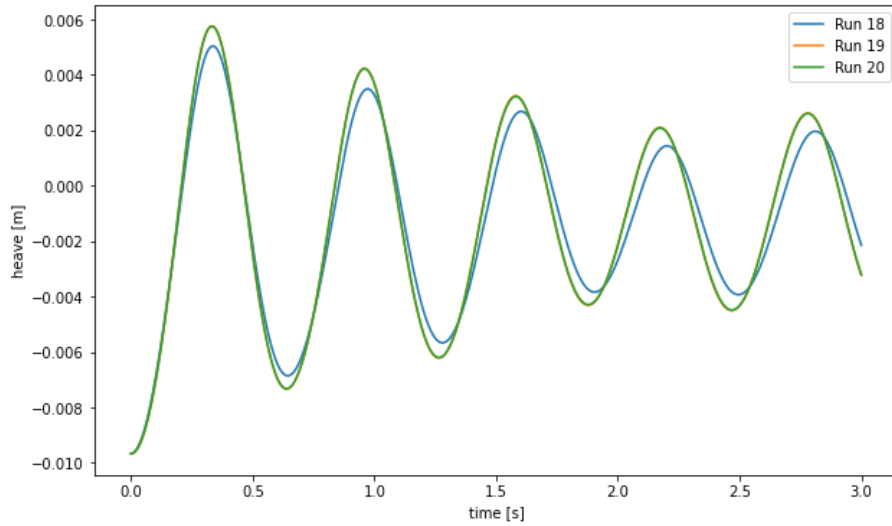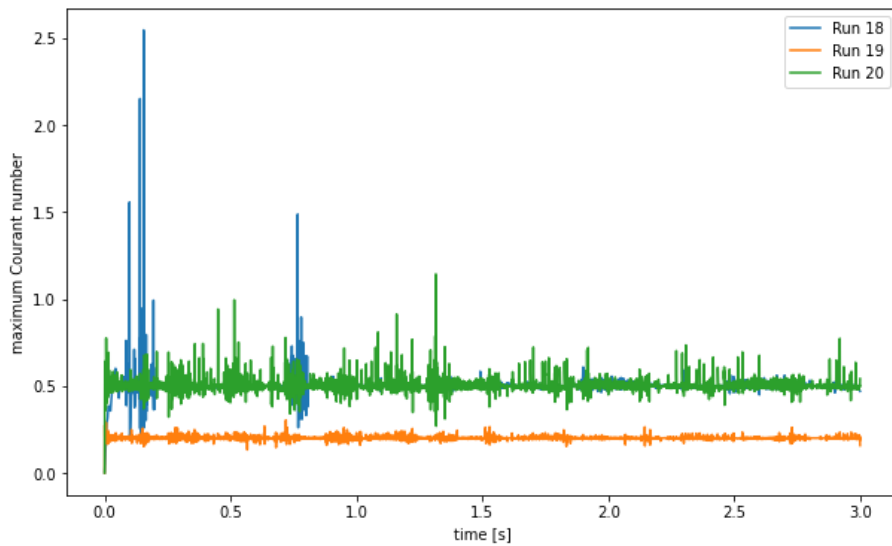Figure 4.38: Maximum Courant number comparison between run cases 18, 19 and 20.
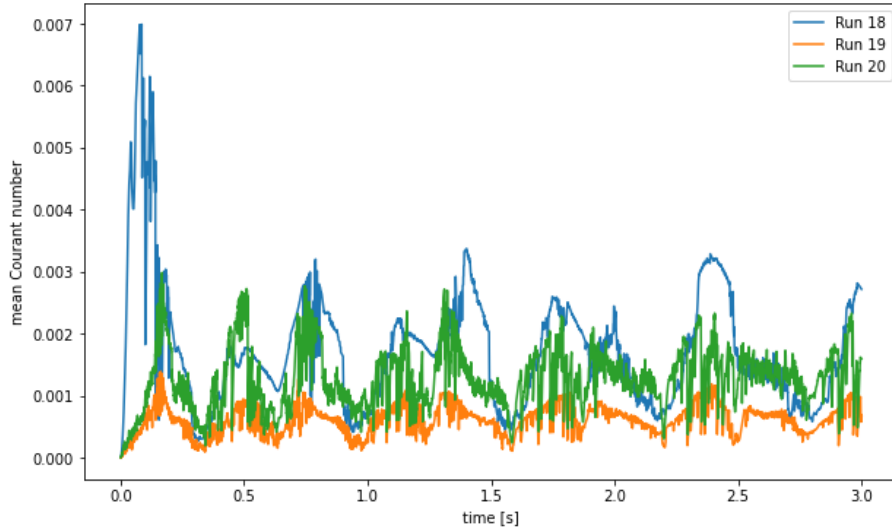
Figure 4.39: Mean Courant number comparison between run cases 18, 19 and 20.

mesh	E
inner warping distance	0.05
outer warping distance	0.1
turbulence model	k-omega SST
surface tension	$0.0728\,\mathrm{N\,m^{-1}}$
k	$0.01\,\mathrm{m^2\,s^{-2}}$
ω	$0.001\,\mathrm{s^{-1}}$
turbulence intensity	0.01
turbulence length scale	0.01
rigid body acceleration relaxation	0.7
schemes as in Table 4.5	
PIMPLE as in Table 4.3	
control	
maximum Courant number	0.5
maximum alpha Courant number	0.5

Table 4.21: Settings for the run 21.

Run 21

Run case 21 results illustrate the impact of increasing initial internal field value of k. The value was risen from 0.001 to 0.01. The simulation performed 43740 PIMPLE iterations, taking $14\,937\,\mathrm{s}$.

Run 22

Run case 22 results show the impact of changing the initial internal field value of ω. The value was risen from 0.001 to 0.01. The simulation performed 42725

mesh	E
inner warping distance	0.05
outer warping distance	0.1
turbulence model	k-omega SST
surface tension	$0.0728\,\mathrm{N\,m^{-1}}$
k	$0.001\,\mathrm{m^2\,s^{-2}}$
ω	$0.01\,\mathrm{s^{-1}}$
turbulence intensity	0.01
turbulence length scale	0.01
rigid body acceleration relaxation	0.7
schemes as in Table 4.5	
PIMPLE as in Table 4.3	
control	
maximum Courant number	0.5
maximum alpha Courant number	0.5

Table 4.22: Settings for the run 22.

mesh	E
inner warping distance	0.05
outer warping distance	0.1
turbulence model	k-omega SST
surface tension	$0.076\,\mathrm{N\,m^{-1}}$
k	$0.001\,\mathrm{m^2\,s^{-2}}$
ω	$0.001\,\mathrm{s^{-1}}$
turbulence intensity	0.01
turbulence length scale	0.01
rigid body acceleration relaxation	0.7
schemes as in Table 4.5	
PIMPLE as in Table 4.3	
control	
maximum Courant number	0.5
maximum alpha Courant number	0.5

Table 4.23: Settings for the run 23.

PIMPLE iterations, taking $13\,985\,\mathrm{s}$.

Run 23

Run case 23 results picture the impact of changing the surface tension coefficient σ value. The coefficient value was risen from $0.0728\,\mathrm{N\,m^{-1}}$ to $0.076\,\mathrm{N\,m^{-1}}$. The simulation performed 44800 PIMPLE iterations, taking $14\,258\,\mathrm{s}$.

Run 24

Run case 24 results present the impact of increasing the turbulence intensity value from 0.01 to 0.05. The simulation performed 46050 PIMPLE iterations,

mesh	E
inner warping distance	0.05
outer warping distance	0.1
turbulence model	k-omega SST
surface tension	$0.0728\,\mathrm{N\,m^{-1}}$
k	$0.001\,\mathrm{m^2\,s^{-2}}$
ω	$0.001\,\mathrm{s^{-1}}$
turbulence intensity	0.05
turbulence length scale	0.01
rigid body acceleration relaxation	0.7
schemes as in Table 4.5	
PIMPLE as in Table 4.3	
control	
maximum Courant number	0.5
maximum alpha Courant number	0.5

Table 4.24: Settings for the run 24.

mesh	E
inner warping distance	0.05
outer warping distance	0.1
turbulence model	k-omega SST
surface tension	$0.0728\,\mathrm{N\,m^{-1}}$
k	$0.001\,\mathrm{m^2\,s^{-2}}$
ω	$0.001\,\mathrm{s^{-1}}$
turbulence intensity	0.01
turbulence length scale	0.05
rigid body acceleration relaxation	0.7
schemes as in Table 4.5	
PIMPLE as in Table 4.3	
control	
maximum Courant number	0.5
maximum alpha Courant number	0.5

Table 4.25: Settings for the run 25.

taking $14\,661\,\mathrm{s}$.

Run 25

The last run case tested the simulation against higher turbulence length scale value. 0.05 was utilised instead of 0.01. That change impacted the simulation in the exactly same way as the change implemented in run case 24. The simulation performed 46050 PIMPLE iterations, taking $14\,907\,\mathrm{s}$.

CHAPTER 5

Summary

This thesis focuses on studying iceberg dynamics and computational fluid dynamics to create comprehensive software that simulates how icebergs behave in the ocean. The process began with an experiment that gathered empirical data, including three tests that involved a cylinder released beneath the water's surface.

This study performed an extensive analysis of the experimental data, described various numerical approaches and chose one of them. Moreover, utilising that numerical approach, various simulation and mesh parameters were tested for stability and various configurations of numerical schemes, and solvers were compared against each other.

5.1 Methodology

OpenFOAM was chosen as the framework adequate for this task. The simulations were performed using the interFoam application with the PIMPLE algorithm. The simulations are grouped into three sections:

- mesh refinement analysis,

- simulation stability analysis on a case based on the experiment's documentation,

- turbulence model analysis using parameters based on the analysis of the empirical data.

Based on this paper, all the source code and analysing tools were published for future research. The repository containing all the frameworks is described in Appendix B. All the numbered simulation run cases are accompanied by the number of PIMPLE iterations performed and the simulation execution time. The simulations were executed by decomposition into 16 subprocesses. The computations utilised CPU AMD Ryzen 7 4800H with 16 logical processors, a mean clock frequency of $3.8\,\text{GHz}$ and $32\,\text{GB}$ of RAM. The machine performed other minor activities in the background. Thus, the execution time may be higher than expected, and the performance may vary between the runs.
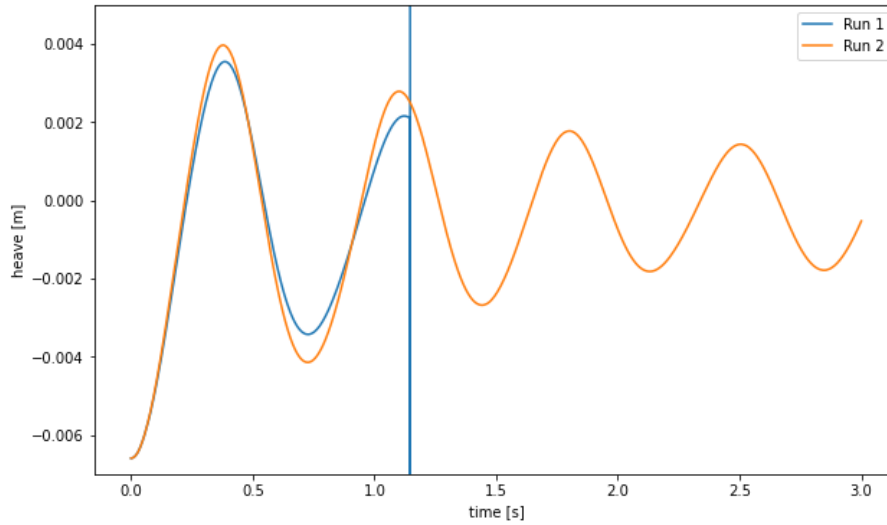
Figure 5.1: Heave time series comparison between run cases 1 and 2. The first one diverges abruptly after $1.146\,34\,\text{s}$.

5.2 Results and analysis

Over two hundred simulations were performed within the scope of this thesis. Only twenty-nine most relevant are presented and analysed. Except for the first four run cases, all the cases are numbered. These include:

- four unnumbered simulations presenting and explaining the process of mesh refinement using the snappyHexMesh tool,

- eight (1 to 8) showing potential problems and improvements when fine-tuning the simulation parameters,

- twelve (9 to 20) presenting four turbulence models. Each was performed thrice, once without surface tension effects and twice with surface tension effects with low (0.2) and high (0.5) maximum Courant number cap.

- five (21 to 25) illustrating the impact of modifying the values of chosen parameters.

Convergence conditions

One of the most important parameters concerning the convergence is the Courant-Friedrichs-Lewy condition. The CFL can be altered by setting the PIMPLE iteration maximum Courant number and the coefficient for the time schemes. Run case 1 showed the importance of limiting the maximum Courant number to avoid feedback loops leading to severe divergences.

Figure 5.1 illustrates the slow divergence in heave motion between run cases 1 and 2. A higher maximum Courant number cap led to repeated exceeding of the limit and finally to a sudden feedback loop-driven singularity (refer
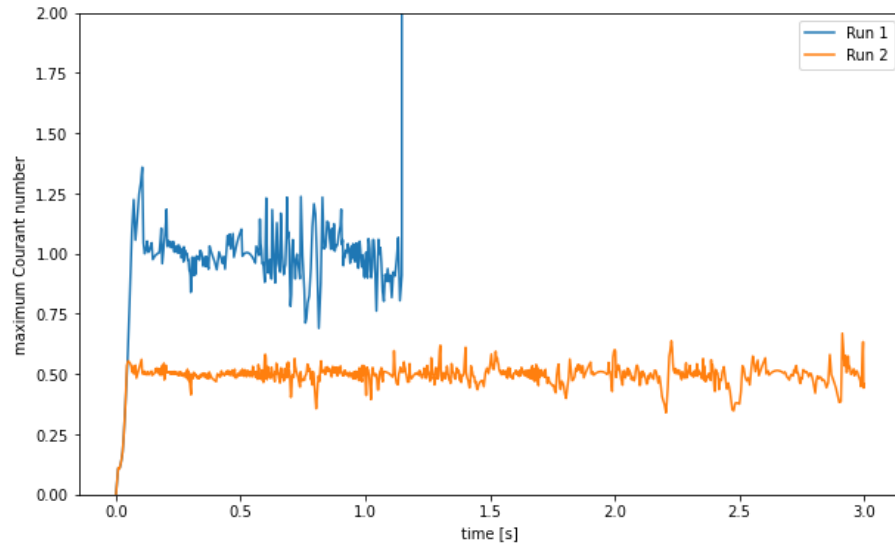
57

Figure 5.2: Maximum Courant number comparison between run cases 1 and 2. The maximum Courant number in run case 1 was capped at 1 and in run case 2 at 0.5.
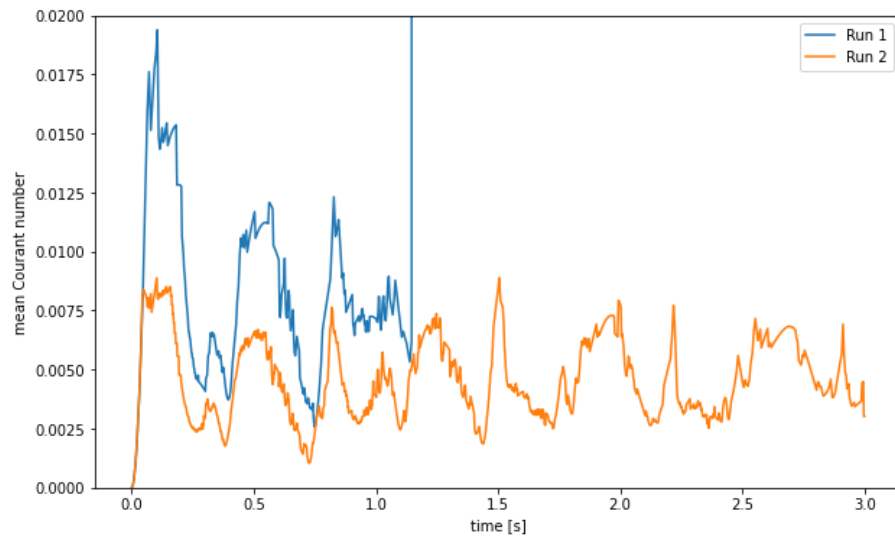

Figure 5.3: Mean Courant number number comparison between run cases 1 and 2.
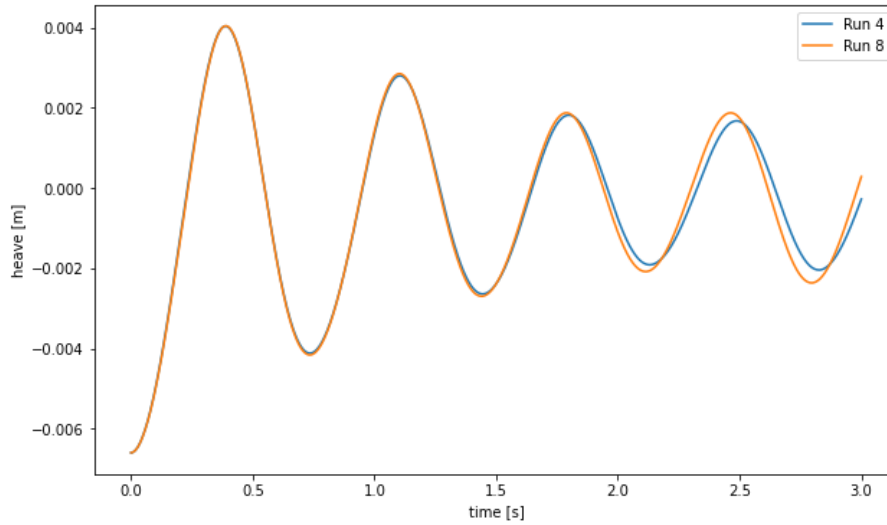
Figure 5.4: Heave time series comparison between run cases 4 and 8. Run case 8 differs by having CFL for Crank-Nicolson time scheme set to 0.9 instead of 0.5.

to Figure 5.2). As shown in Figure 5.3, the maximum Courant number spikes were localised as the mean value oscillated around 0.01.

Similarly, setting the CFL parameter to 1 in run case 8 led to rapid divergence. CFL of 0.9 led to frequent exceeding of the safe Courant number cap of 1 (as seen in Figure 4.23) and resulted in visible result changes (refer to Figure 5.4). Guerrero 2022 advises using low values of CFL < 0.9, and the simulation cases discussed by Kramer et al. 2021 employed the value of 0.5.

Further recommendations by Guerrero 2022 included setting higher numbers of correctors and using different schemes. The transition between run cases 2 and 3 showed the impact of the correctors. However, the schemes advised by Guerrero 2022, compared with run cases 3 and 4, seem not to change anything as the results were identical, only varying execution time, which could have resulted from different processor resources accessibility.

Mesh refinement

Run cases 4, 5, 6 and 7 showed the impact of different grading and refinement on the simulation results. As presented in Figure 4.22, the most significant impact resulted from too little refinement around the water surface, leading to a considerably shifted equilibrium point. Moreover, higher mesh refinement around the cylinder led to higher damping. More research is needed to analyse the impact of mesh refinement on the simulation depending on various parameters. Overrefinned mesh may result in too high cell size differences and, thus, in numerical errors. Underrefined mesh may result in loss of near-surface effects. Because of time and computation resource limitations, the refinement levels of mesh 'B' followed in the remaining simulations.
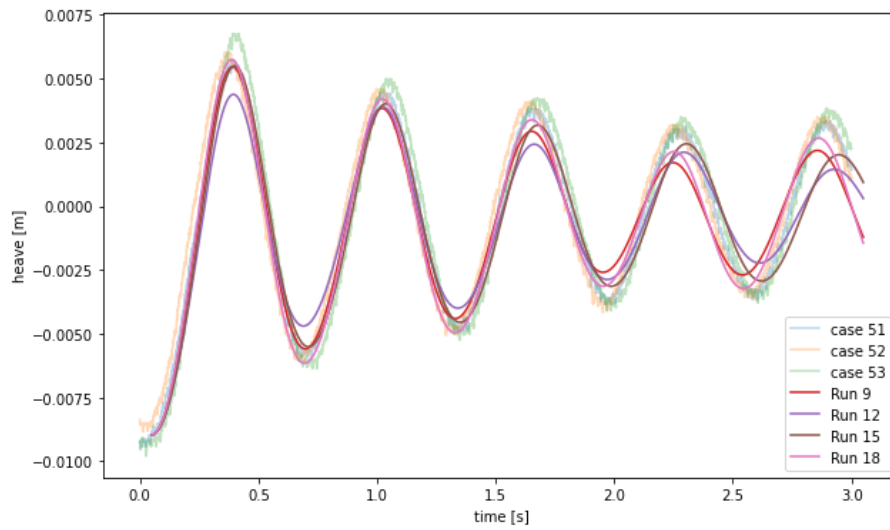
Figure 5.5: Heave time series comparison between run cases 9, 12, 15 and 18, representing the no surface tension model. The series are compared with the experimental results.
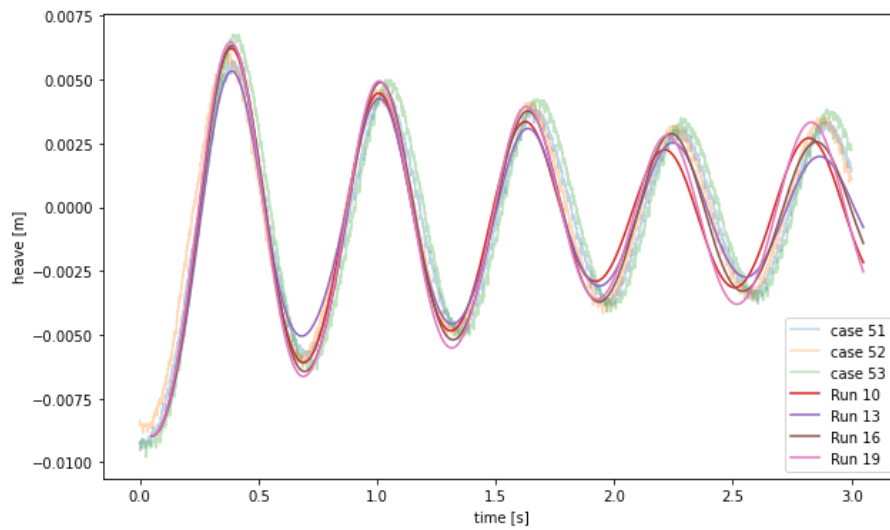

Figure 5.6: Heave time series comparison between run cases 10, 13, 16 and 19, representing the low Courant number model with surface tension. The series are compared with the experimental results.

Turbulence model comparison

Run cases 9 through 20 compared four turbulence models: k-ϵ, k-ω, k-ω SST and laminar. Each was employed against three sets of parameters: $\sigma = 0\,\mathrm{N\,m^{-1}}, \mathrm{maxCo} = 0.2$, $\sigma = 0.0728\,\mathrm{N\,m^{-1}}, \mathrm{maxCo} = 0.2$ and $\sigma = 0.0728\,\mathrm{N\,m^{-1}}, \mathrm{maxCo} = 0.5$. Only the laminar case utilised the maximum Courant number limit of 0.5 for the case without surface tension.
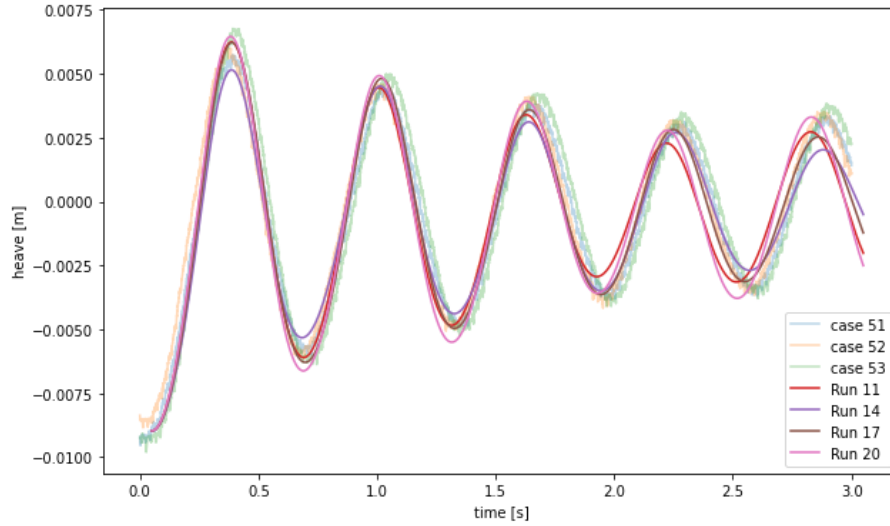
Figure 5.7: Heave time series comparison between run cases 11, 14, 17 and 20, representing the high Courant number model with surface tension. The series are compared with the experimental results.
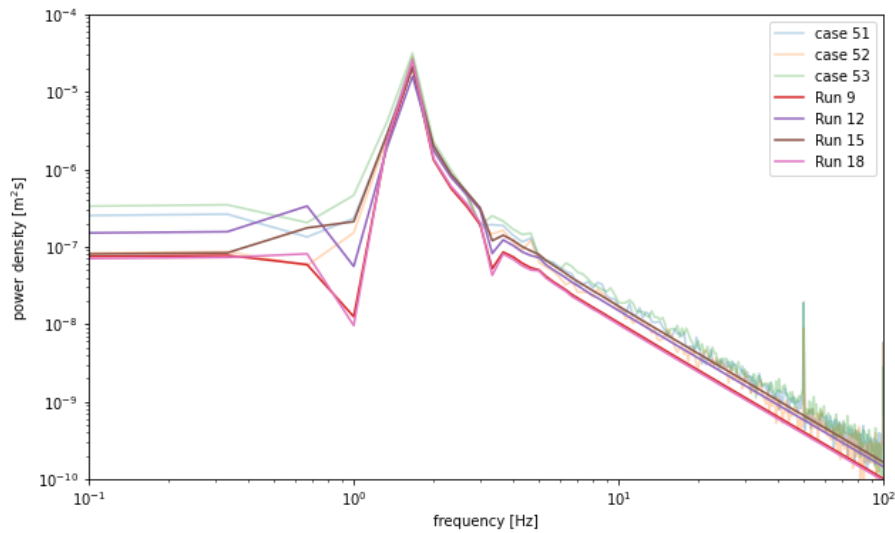

Figure 5.8: Power spectral density comparison between run cases 9, 12, 15 and 18, representing the no surface tension model, and the experimental data.
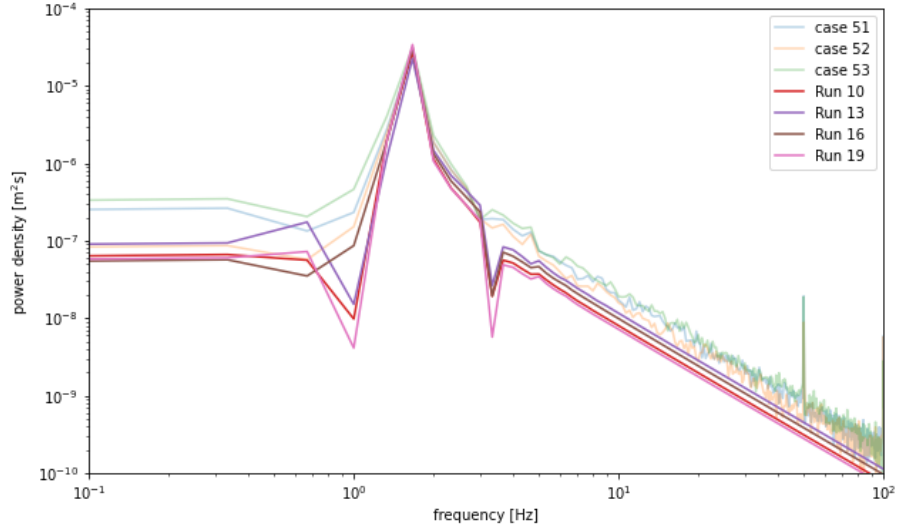
Figure 5.9: Power spectral density comparison between run cases 10, 13, 16 and 19, representing the low Courant number model with surface tension, and the experimental data.
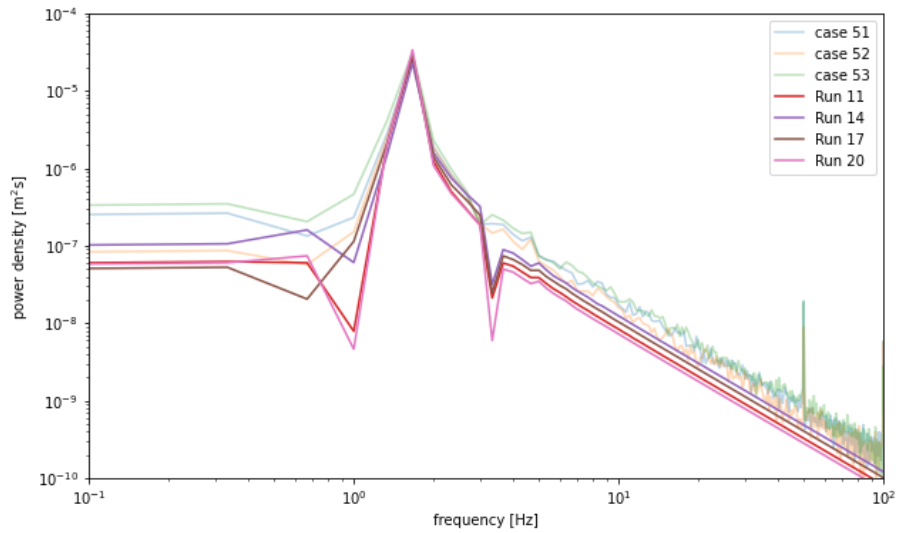

Figure 5.10: Power spectral density comparison between run cases 11, 14, 17 and 20, representing the high Courant number model with surface tension, and the experimental data.

Figures 5.5 to 5.7 illustrate the significance of the surface tension effects in such small scales. In all cases, k-ω models overdamped, leading to divergence from the empirical data. On the other hand, k-ω SST reproduces the heave motion for both the low and high Courant number cases correctly. The difference appears in the last 0.5 s due to the wave reflection in the experimental data, which does not occur in the simulation with the k-ω SST model.

Notably, the laminar model is the best at recreating the heave motion amplitude, including the final wave reflection impact. However, that model fails with proper frequency reproduction and results in too fast oscillation.

All models produce an amplitude fall at around 2 Hz (refer to Figures 5.8 to 5.10). Such a fall does not exist in the experimental data. A similar drop can be observed at 1 Hz in all models except k-ω SST. Again, such a fall does not appear in the experimental data. All models fail at reproducing the lower frequencies. However, these may result from the initial unstable state of the water in the tank. Thus, they may not be correctly reproducible from an initially static state.

Higher frequencies have lower amplitudes in the simulation run cases than in the experimental data. However, this difference may result from the sensor noises and the impact of the sound in the laboratory.

Despite much higher Courant numbers, run cases 11, 14, 17 and 20 do not differ significantly from their low Courant number counterparts. For the k-ϵ and laminar cases, the low-frequency fall is less pronounced, and for k-*omega* SST, the low-frequency fall is shifted towards even lower frequencies. The k-*omega* case has a much less pronounced low-frequency fall. The differences in higher frequencies are barely visible.

Parameters tuning

The last set of simulations included the k-ω SST model with five different alterations:

- Run case 21 - ten times higher initial value of k,

- Run case 22 - ten times higher initial value of ω,

- Run case 23 - higher surface tension coefficient, $0.076 \, \text{N m}^{-1}$ instead of $0.0728 \, \text{N m}^{-1}$,

- Run case 24 - five times higher turbulence intensity,

- Run case 25 - five times higher turbulence length scale.

Run case 17 was chosen as the comparison base. It included surface tension effects and used a higher Courant number cap. Figures 5.11 and 5.13 illustrate the difference between the nominal and altered run cases.

There is no visible change for altering either turbulence intensity or turbulence length scale. These parameters characterise the initial state of turbulence relative to the initial velocity. The velocity in the initial frame is zero, thus no change.

Increasing either k and ω values increases damping and lowers the oscillation frequency. It is evident in Figure 5.12, where cases 21 and 22 have visibly higher
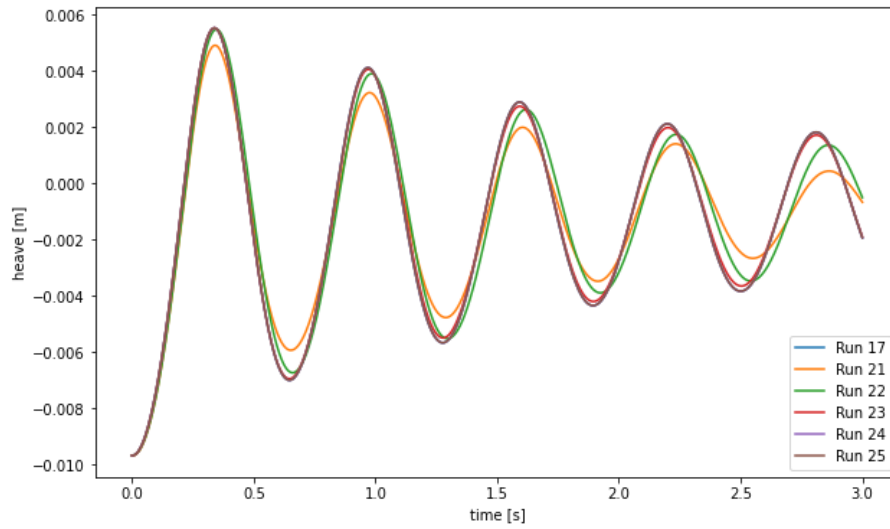
Figure 5.11: Heave time series comparison between the base run case 17 and its modifications, run cases 21 through 25.
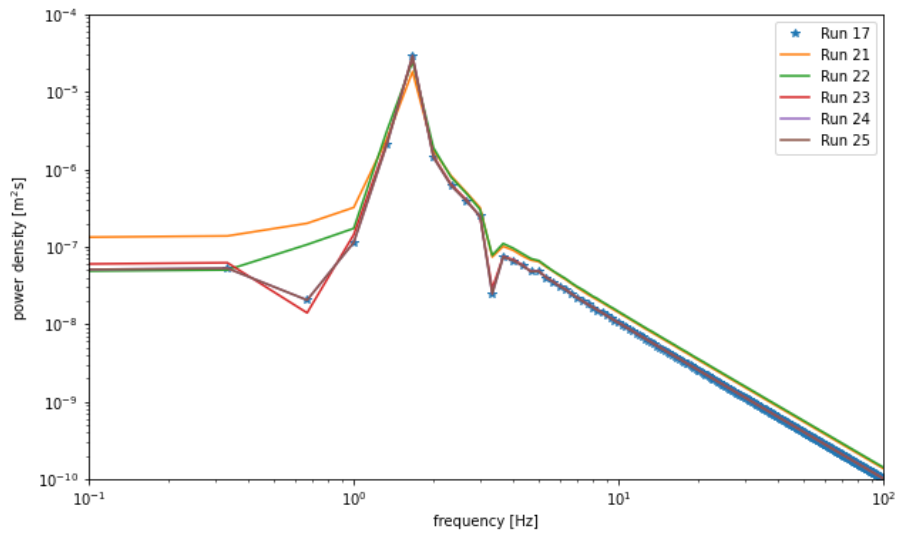

Figure 5.12: Power spectral density comparison between the base run case 17 and its modifications, run cases 21 through 25.
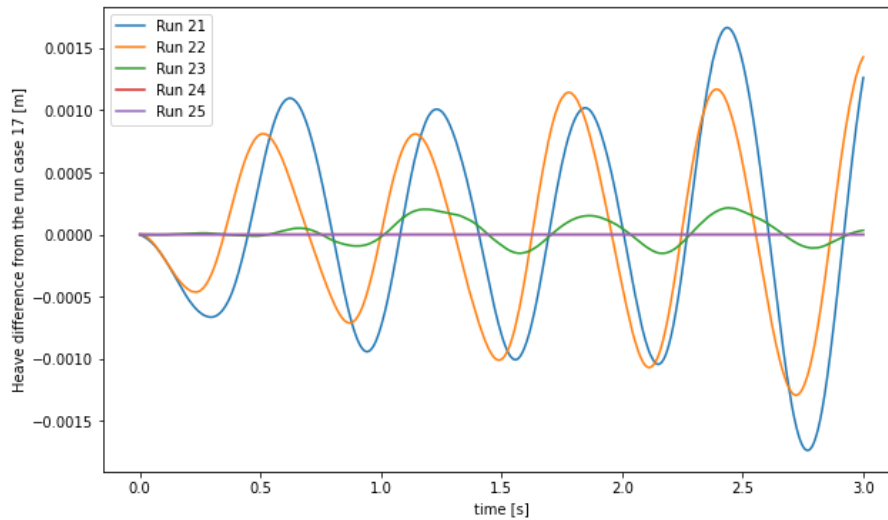
Figure 5.13: Heave difference between the modification run cases 21 through 25, and run case 17.

amplitude, around $0.67\,\mathrm{Hz}$. Interestingly, increasing the k impacts notably the very low frequencies. Both these runs display the impact of the initial turbulence on the damping.

Because of the initial static state and theoretical lack of turbulence, both values should be as close to zero as possible, and any alteration should have minimal to no impact. More simulations should follow to estimate the reasonable values for both k and ω, as the values chosen may still need to be lowered.

The last change is a slight increase in surface tension. Slightly more intensive damping occurs, and the amplitude drop at around $0.67\,\mathrm{Hz}$ is more pronounced than in the nominal case. Much less pronunciation is visible in Figures 5.8 to 5.10. It may mean the surface tension of the water in the experiment was lower than that assumed for the experiment. Lower surface tension may result from higher temperatures (refer to The Engineering ToolBox 2004) or from pollutants in water.

5.3 Conclusion

This study analysed the possibility of simulating the heave of a buoyant cylinder within a very low Reynolds number domain. The k-ω SST model proved to perform correctly and efficiently when simplifying the problem to only two dimensions. The survey results are consistent with hitherto published research and provide a proper basis for further development. The successive study should include more complex problems, like farther initial displacement, waves or more complex geometries. Moreover, it should also analyse the possibilities of improving the simulation quality by using sliding meshes or the `oversetMesh` functionality. Because of minimal motion, these were not required to use within this paper's work.

5.4   Contribution

Most research topics within similar fields concern either high relative velocity or large scales. The results and findings of this paper may form a proper foundation for any future study, including low Reynolds flows, viscous effects and the viscosity impact on scalability. It may also be employed as a reference for future experiments and their numerical reconstruction.

Furthermore, this paper describes various steps performed in preparing the simulation setup. All the code and tools used for the analysis are published and easily accessible. These may accelerate the progress of any future study struggling with finding a proper foundation.

5.5   Limitations

Only three experimental data sets with limited descriptions and documentation were provided. The experiments were performed on a wax candle with an uneven surface. No density measurements were performed. Little to no water or air measurements were conducted. These factors may have strongly impacted the experimental results. Thus, the numerical reconstruction might have used the wrong parameters, leading to observed errors and inconsistencies.

All of this research was performed as a part of a short master's thesis. Such theses are highly time-limited, not giving enough time for thorough research. Moreover, only one machine was utilised for the simulations, significantly limiting the simulation data obtained.

5.6   Future works

This study was one of the first steps within a more protracted process of developing a good iceberg simulator. Further studies should analyse the experimental data and compare them to various simulation setups for bodies released from above the water surface. Moreover, the impact of an unsteady initial state should be studied. Furthermore, other geometries, for example, three-dimensional objects with uneven surfaces, should be utilised.

The succeeding research should employ the results of this thesis to assess the adequate configurations. Other studies that would analyse less static cases should compare the accuracy of the models used in this paper and decide whether they can be utilised in the final simulator.

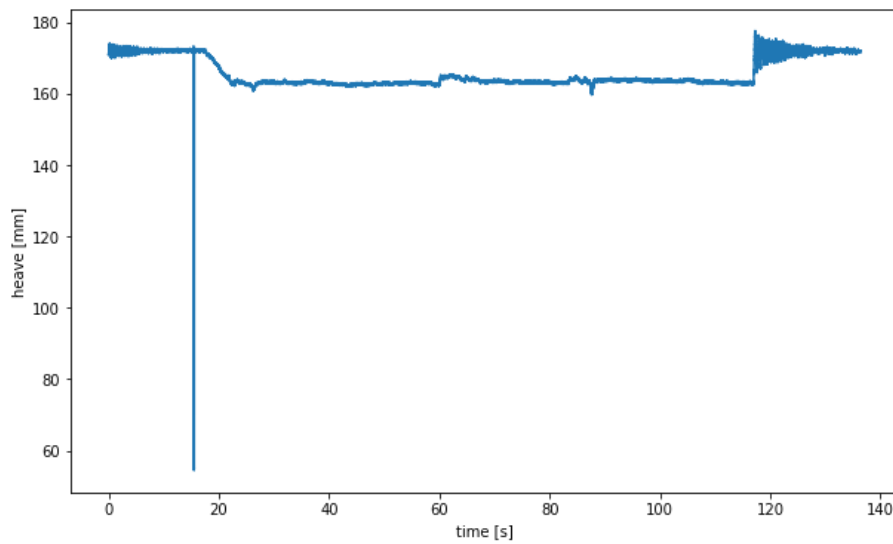# Appendices

APPENDIX A

Experimental data

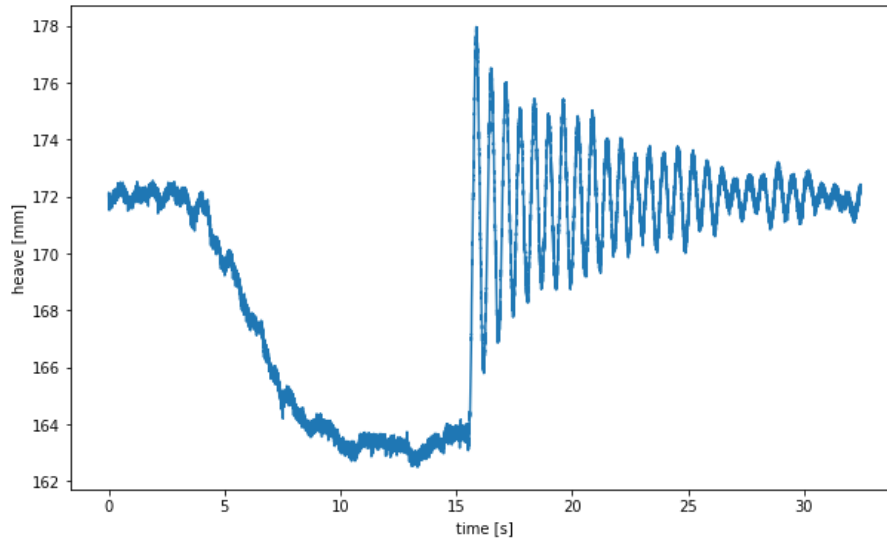Figure A.1: Time series for experiment '51', fully submerged cylinder

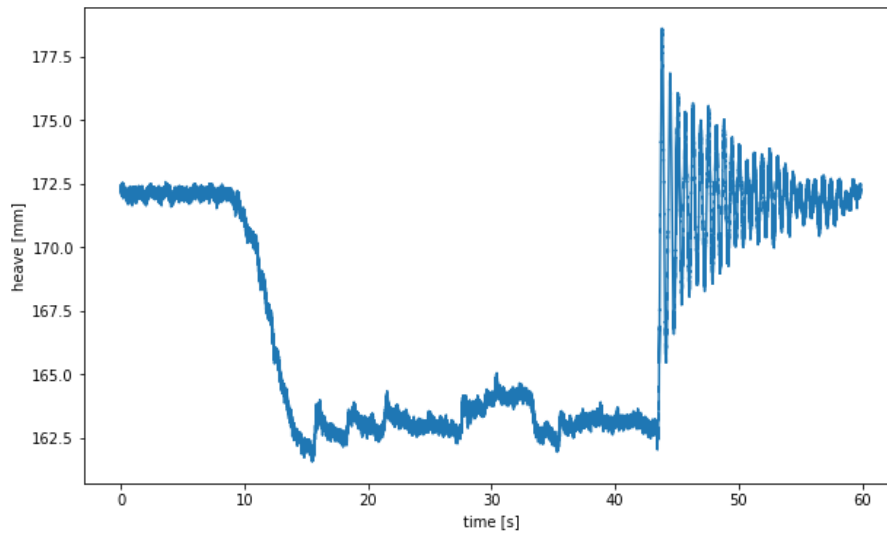Figure A.2: Time series for experiment '52', fully submerged cylinder

Figure A.3: Time series for experiment '53', fully submerged cylinder
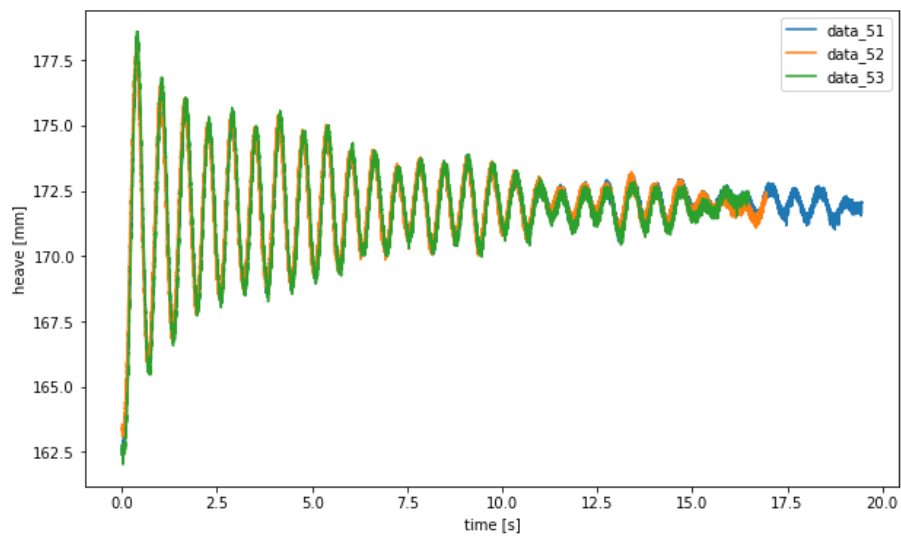
Figure A.4: Comparison of heave time series for experiments '51', '52' and '53'. Time series trimmed to the moment of release.

APPENDIX B

Repository structure
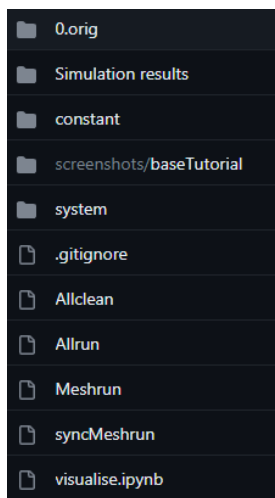
(a) Main repository folder.
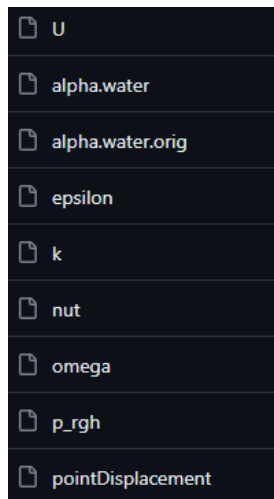
(b) 0.orig folder containing the initial simulation field values.

(c) Repository folder containing all the simulation result log files for the run cases described in this thesis.

(a) constant folder containing the dictionaries with constant entries.

(b) system folder containing the dictionaries with system entries.

Bibliography

Ahmadzadeh, M. et al. (2014). 'Numerical simulation of sphere water entry problem using Eulerian–Lagrangian method'. In: *Applied Mathematical Modelling* vol. 38, no. 5-6, pp. 1673–1684.

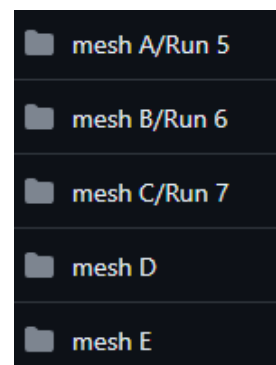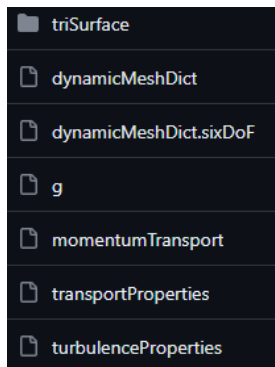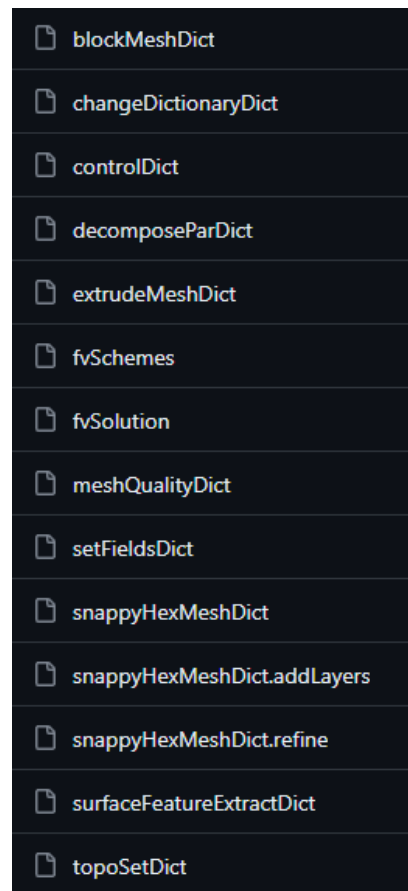Battistin, D. and Iafrati, A. (2003). 'Hydrodynamic loads during water entry of two-dimensional and axisymmetric bodies'. In: *Journal of fluids and structures* vol. 17, no. 5, pp. 643–664.

Calderer, A. et al. (2014). 'Coupled fluid-structure interaction simulation of floating offshore wind turbines and waves: a large eddy simulation approach'. In: *Journal of Physics: Conference Series.* Vol. 524. 1. IOP Publishing, p. 012091.

CFD Direct Ltd (2015–2023). *OpenFOAM® multiphase flow solvers.* URL: https://cfd.direct/openfoam/features/multiphase/ (visited on 31/01/2023).

Crank, J. and Nicolson, P. (1947a). 'A practical method for numerical evaluation of solutions of partial differential equations of the heat-conduction type'. In: *Mathematical Proceedings of the Cambridge Philosophical Society* vol. 43, no. 1, pp. 50–67.

Crank, J. and Nicolson, P. (1947b). 'A practical method for numerical evaluation of solutions of partial differential equations of the heat-conduction type'. In: *Mathematical proceedings of the Cambridge philosophical society.* Vol. 43. 1. Cambridge University Press, pp. 50–67.

Devolder, B. et al. (Sept. 2015). 'A Review of the Implicit Motion Solver Algorithm in OpenFOAM® to Simulate a Heaving Buoy'. English. In: 18th Numerical Towing Tank Symposium (NuTTS'15) ; Conference date: 28-09-2015 Through 30-09-2015.

Eldredge, J. D. (2007). 'Numerical simulation of the fluid dynamics of 2D rigid body motion with the vortex particle method'. In: *Journal of Computational Physics* vol. 221, no. 2, pp. 626–648.

Elias, A. C. (2015). 'Fluid-structure interaction simulation of complex floating structures and waves'. PhD thesis. University of Minnesota.

Fornberg, B. (1973). 'On the instability of leap-frog and Crank-Nicolson approximations of a nonlinear partial differential equation'. In: *Mathematics of Computation* vol. 27, no. 121, pp. 45–57.

Gilmanov, A. and Acharya, S. (2008). 'A hybrid immersed boundary and material point method for simulating 3D fluid–structure interaction problems'. In: *International journal for numerical methods in fluids* vol. 56, no. 12, pp. 2151–2177.

Gilmanov, A. and Sotiropoulos, F. (2005). 'A hybrid Cartesian/immersed boundary method for simulating flows with 3D, geometrically complex, moving bodies'. In: *Journal of computational physics* vol. 207, no. 2, pp. 457–492.

Greenhow, M. (1987). 'Wedge entry into initially calm water'. In: *Applied Ocean Research* vol. 9, no. 4, pp. 214–223.

— (1988). 'Water-entry and-exit of a horizontal circular cylinder'. In: *Applied Ocean Research* vol. 10, no. 4, pp. 191–198.

Guerrero, J. (Mar. 2022). 'OpenFOAM advanced training. Moving meshes, rigid body motion, adaptive mesh refinement, and overset meshes'. In.

Henry, B. (2013). *Immersed boundary methods.*

Itō, S. (1977). 'Study of the transient heave oscillation of a floating cylinder.' PhD thesis. Massachusetts Institute of Technology.

Keghouche, I., Bertino, L. and Lisæter, K. A. (2009). In: *Journal of Atmospheric and Oceanic Technology.*

Kramer, M. B. et al. (2021). 'Highly accurate experimental heave decay tests with a floating sphere: A public benchmark dataset for model validation of fluid–structure interaction'. In: *Energies* vol. 14, no. 2, p. 269.

Lewis, S. G. et al. (2010). 'Impact of a free-falling wedge with water: synchronized visualization, pressure and acceleration measurements'. In: *Fluid Dynamics Research* vol. 42, no. 3, p. 035509.

Li, H. and Bachynski, E. E. (2019). 'Numerical Simulation of Fully Nonlinear Interaction Between Regular and Irregular Waves and a 2D Floating Body'. In: *International Conference on Offshore Mechanics and Arctic Engineering.* Vol. 58844. American Society of Mechanical Engineers, V07AT06A028.

Lichey, Harmut and Hellmer (2001). In: *journal of glaciology* vol. 47.

Lin, P. (2007). 'A fixed-grid model for simulation of a moving body in free surface flows'. In: *Computers & fluids* vol. 36, no. 3, pp. 549–561.

May, A. (1951). 'Effect of surface condition of a sphere on its water-entry cavity'. In: *Journal of Applied Physics* vol. 22, no. 10, pp. 1219–1222.

Mei, X., Liu, Y. and Yue, D. K. (1999). 'On the water impact of general two-dimensional sections'. In: *Applied Ocean Research* vol. 21, no. 1, pp. 1–15.

Menter, F. R., Kuntz, M. and Langtry, R. (2003). 'Ten years of industrial experience with the SST turbulence model'. In: *Turbulence, heat and mass transfer* vol. 4, no. 1, pp. 625–632.

Moctar, O. el, Shigunov, V. and Zorn, T. (2012). 'Duisburg Test Case: Post-Panamax Container Ship for Benchmarking'. In: *Ship Technology Research* vol. 59, no. 3, pp. 50–64. eprint: https://doi.org/10.1179/str.2012.59.3.004.

Moyo, S. and Greenhow, M. (2000). 'Free motion of a cylinder moving below and through a free surface'. In: *Applied Ocean Research* vol. 22, no. 1, pp. 31–44.

Newmark, N. M. (1959). 'A method of computation for structural dynamics'. In: *Journal of the engineering mechanics division* vol. 85, no. 3, pp. 67–94.

Nguyen, V.-T., Ha, C.-T. and Park, W.-G. (2013). 'Multiphase flow simulation of water-entry and-exit of axisymmetric bodies'. In: *ASME International Mechanical Engineering Congress and Exposition.* Vol. 56314. American Society of Mechanical Engineers, V07AT08A063.

Norsk Petroleum (2023). *Activity per sea area.* https://www.norskpetroleum. no/en/developments-and-operations/activity-per-sea-area. Accessed: 2023-04-28.

Odorczuk, M. J. and Chanrion, H. (Dec. 2022). 'Simulating drift tracks of icebergs in the Barents Sea'. Report for AT327 course at UNIS.

Online, C. (2011). *K-epsilon models.* https://www.cfd-online.com/Wiki/K-epsilon_models. [Online; accessed 10-March-2023].

— (2014). *Turbulence free-stream boundary conditions.* https://www.cfd-online.com/Wiki/Turbulence_free-stream_boundary_conditions. [Online; accessed 06-May-2023].

— (2022). *Turbulence intensity.* https://www.cfd-online.com/Wiki/Turbulence_intensity. [Online; accessed 06-May-2023].

— (2023). *Computational Fluid Dynamics reference.* https://www.cfd-online.com/Wiki. [Online; accessed 06-May-2023].

OpenCFD (2023). *OpenFOAM User Guide.* URL: http://www.openfoam.org/ (visited on 10/05/2023).

OpenFOAM Foundation (2018). *smoothSolver Class reference - OpenFOAM: The Open Source CFD Toolbox.* URL: https://cpp.openfoam.org/v5/classFoam_1_1smoothSolver.html (visited on 11/03/2023).

OpenFOAM Wiki Contributors (2021). *The PIMPLE algorithm in OpenFOAM.* https://openfoamwiki.net/index.php/OpenFOAM_guide/The_PIMPLE_algorithm_in_OpenFOAM. Accessed: 2023-03-12.

Popinet, S. et al. (2013–2023). *Basilisk.* URL: http://basilisk.fr/ (visited on 31/01/2023).

Seng, S., Jensen, J. J. and Malenica, Š. (2014). 'Global hydroelastic model for springing and whipping based on a free-surface CFD code (OpenFOAM)'. In: *International Journal of Naval Architecture and Ocean Engineering* vol. 6, no. 4, pp. 1024–1040.

Shen, L., Chan, E.-S. and Lin, P. (2009). 'Calculation of hydrodynamic forces acting on a submerged moving object using immersed boundary method'. In: *Computers & Fluids* vol. 38, no. 3, pp. 691–702.

Spalding, D. B. (1972). 'A novel finite difference formulation for differential expressions involving both first and second derivatives'. In: *International Journal for Numerical Methods in Engineering* vol. 4, no. 4, pp. 551–559.

Sun, T. et al. (2021). 'Experimental study on the influence of the angle of attack on cavity evolution and surface load in the water entry of a cylinder'. In: *Ocean Engineering* vol. 219, p. 108271.

Surface Tension (2017). *Surface tension values of some common test liquids for surface energy analysis.* http://www.surface-tension.de. Accessed: 2023-05-09.

Takamure, K. and Uchiyama, T. (2020). 'Air–water interface dynamics and energy transition in air of a sphere passed vertically upward through the interface'. In: *Experimental Thermal and Fluid Science* vol. 118, p. 110167.

The Engineering ToolBox (2004). *Surface Tension of Water in contact with Air.* https://www.engineeringtoolbox.com/water-surface-tension-d_597.html. Accessed: 2023-05-14.

The OpenFOAM Foundation Ltd (2011–2023). *OpenFOAM®.* URL: https://www.openfoam.com/documentation/user-guide (visited on 31/01/2023).

Truscott, T. T., Epps, B. P. and Munns, R. H. (2016). 'Water exit dynamics of buoyant spheres'. In: *Physical Review Fluids* vol. 1, no. 7, p. 074501.

van Leer, B. (1974). 'Towards the ultimate conservative difference scheme. II. Monotonicity and conservation combined in a second-order scheme'. In: *Journal of Computational Physics* vol. 14, no. 4, pp. 361–370.

Wilcox, D. C. et al. (1998). *Turbulence modeling for CFD*. Vol. 2. DCW industries La Canada, CA.

Wu, G., Sun, H. and He, Y. (2004). 'Numerical simulation and experimental study of water entry of a wedge in free fall motion'. In: *Journal of Fluids and Structures* vol. 19, no. 3, pp. 277–289.

Wu, Q. et al. (2017). 'Experimental study on large deformation of free surface during water exit of a sphere'. In: *Ocean Engineering* vol. 140, pp. 369–376.

Yang, J. and Stern, F. (2009). 'Sharp interface immersed-boundary/level-set method for wave–body interactions'. In: *Journal of Computational Physics* vol. 228, no. 17, pp. 6590–6616.

Zhao, R. and Faltinsen, O. (1993). 'Water entry of two-dimensional bodies'. In: *Journal of fluid mechanics* vol. 246, pp. 593–612.